# The 2018 unrest phase at La Soufrière of Guadeloupe (French West Indies) andesitic volcano: Scrutiny of a failed but prodromal phreatic eruption

Roberto Moretti [a,b,*], Jean-Christophe Komorowski [a], Guillaume Ucciani [a,b], Séverine Moune [a,b,c], David Jessop [a,b,c], Jean-Bernard de Chabalier [a], François Beauducel [a,d], Magali Bonifacie [a,b], Arnaud Burtin [a,b], Martin Vallée [a], Sebastien Deroussi [a,b], Vincent Robert [a,b], Dominique Gibert [e], Tristan Didier [a,b], Thierry Kitou [a,b], Nathalie Feuillet [a], Patrick Allard [a], Giancarlo Tamburello [f], Tara Shreve [a], Jean-Marie Saurel [a], Arnaud Lemarchand [a], Marina Rosas-Carbajal [a], Pierre Agrinier [a], Anne Le Friant [a], Marc Chaussidon [a]

[a] Université de Paris, Institut de physique du globe de Paris, CNRS, F-75005 Paris, France
[b] Observatoire volcanologique et sismologique de Guadeloupe, Institut de physique du globe de Paris, F-97113 Gourbeyre, France
[c] Université Clermont Auvergne, CNRS, IRD, OPGC, Laboratoire Magmas et Volcans, F-63000 Clermont-Ferrand, France
[d] Institut des Sciences de la Terre - Institut de Recherche pour le Développement - BPPTKG - PVMBG Badan Geologi, Yogyakarta, Indonesia
[e] Geosciences Rennes UMR 6118 - Univ. Rennes I, Rennes, France
[f] Istituto Nazionale di Geofisica e Vulcanologia sezione di Bologna, via Donato Creti, Bologna, Italy

## ARTICLE INFO

## ABSTRACT

After 25 years of gradual increase, volcanic unrest at La Soufrière of Guadeloupe reached its highest seismic energy level on 27 April 2018, with the largest felt volcano-tectonic (VT) earthquake ($M_L$ 4.1 or $M_W$ 3.7) recorded since the 1976–1977 phreatic eruptive crisis. This event marked the onset of a seismic swarm (180 events, 2 felt) occurring after three previous swarms on 3–6 January (70 events), 1 st February (30 events, 1 felt) and 16–17 April (140 events, 1 felt). Many events were hybrid VTs with long-period codas, located 2–4 km below the volcano summit and clustered within 2 km along a regional NW-SE fault cross-cutting La Soufrière. Elastic energy release increased with each swarm whereas inter-event time shortened. At the same time, summit fractures continued to open and thermal anomalies to extend. Summit fumarolic activity increased significantly until 20 April, with a maximum temperature of 111.4 °C and gas exit velocity of 80 m/s, before declining to ~95 °C and ~33 m/s on 25 April. Gas compositions revealed increasing C/S and $CO_2/CH_4$ ratios and indicate hydrothermal P-T conditions that reached the critical point of pure water. Repeated MultiGAS analysis of fumarolic plumes showed increased $CO_2/H_2S$ ratios and $SO_2$ contents associated with the reactivation of degassing fractures (T = 93 °C, $H_2S/SO_2 \approx 1$). While no direct evidence of upward magma migration was detected, we attribute the above phenomena to an increased supply of deep magmatic fluids that heated and pressurized the La Soufrière hydrothermal system, triggering seismogenic hydro-fracturing, and probable changes in deep hydraulic properties (permeability) and drainage pathways, which ultimately allowed the fumarolic fluxes to lower. Although this magmatic fluid injection was modulated by the hydrothermal system, the unprecedented seismic energy release and the critical point conditions of hydrothermal fluids suggest that the 2018 sequence of events can be regarded as a failed phreatic eruption. Should a similar sequence repeat, we warn that phreatic explosive activity could result from disruption of the shallow hydrothermal system that is currently responsible for 3–9 mm/y of nearly radial horizontal displacements within 1 km from the dome. Another potential hazard is partial collapse of the dome's SW flank, already affected by basal spreading above a detachment surface inherited from past collapses. Finally, the increased magmatic fluid supply evidenced by geochemical indicators in 2018 is compatible with magma replenishment of the 6–7 km deep crustal reservoir feeding La Soufrière and, therefore, with a potential evolution of the volcano's activity towards magmatic conditions.

© 2020 Elsevier B.V. All rights reserved.

* Corresponding author at: Université de Paris, Institut de physique du globe de Paris,
CNRS, F-75005 Paris, France.
*E-mail address:* moretti@ipgp.fr (R. Moretti).

## 1. Introduction

Andesitic volcanoes develop hydrothermal systems that hamper a direct interpretation of the subterranean magma state and evolution from the physical and chemical signals measured at the surface. This limitation contributes enormously to the dilemma of whether observed volcanic unrest has a magmatic origin ("magma on the move") or a non-magmatic origin from a change in the hydrothermal system ("fluids that are not magma on the move") (Pritchard et al., 2019) and produces major uncertainties in the short-term forecasting of an imminent eruption. Such uncertainties are severe also for the short-term eruption hazard from non-magmatic unrest, as andesitic volcanoes may develop explosive phreatic eruptions (e.g., Barberi et al., 1992). Characterized by the absence of juvenile magmatic material, phreatic eruptions are triggered by the injection of fluids and heat of magmatic origin into the hydrothermal system, which becomes strongly overpressured (Barberi et al., 1992; Mastin, 1995; Rouwet et al., 2014 and references therein). In many cases phreatic eruptions are precursors to magmatic eruptions of both explosive or effusive nature, or could serve as the decompression mechanism prior to phreatomagmatic eruptions (Rouwet et al., 2014). However, the input of mass and heat into the hydrothermal system challenges monitoring systems, being often a short-term and too low amplitude event that does not result in clear precursory signals within the time frame of monitoring (Barberi et al., 1992; Rouwet et al., 2014). If on one hand the hydrothermal system tends to buffer and mask the inputs of deep hot fluids, on the other side secondary mineral precipitation and the presence of low-permeable elemental sulphur can seal hydrothermal systems in localized, shallow and overpressured portions that can rapidly reach the threshold to phreatic eruptive activity (Salaün et al., 2011; Rouwet et al., 2014). Therefore, it is of the outmost importance to track and understand the anomalies in observation data that are related to the input of deep hot magmatic fluids into the hydrothermal system. The ongoing unrest at La Soufrière explosive andesitic volcano, on the island of Guadeloupe (French West Indies), well represents the aforementioned issues and offers us this possibility.

## 2. Introduction and volcanological background

La Soufrière de Guadeloupe is located in the Lesser Antilles arc under which the Northern Atlantic ocean plate is subducting beneath the Caribbean plate at a rate of ~2 cm/year (Feuillet et al., 2002, 2011). La Soufrière belongs to the Grande Découverte volcanic complex, built during the past 445,000 years and comprising three stratovolcanoes: Grande Découverte, Carmichael and Soufrière (Komorowski et al., 2005). La Soufrière is the most recent volcanic edifice and its eruptive history began about 9150 years ago. It is an active explosive volcano that has experienced magmatic and non-magmatic "phreatic" eruptions, in the past (Komorowski et al., 2005; Feuillard et al., 1983; Legendre, 2012). The most recent major magmatic eruption dates from 1530 CE and began with a collapse of the volcanic edifice causing a landslide that reached the coast 10 km away. The explosive eruption that followed resulted in ash and pumice fallout on southern Basse-Terre, the outpouring of pyroclastic flows (incandescent avalanches of gas, ashes and rocks) that reached distances of 5–7 km from the volcano, and mudflows (Boudon et al., 2008; Komorowski et al., 2008). It ended with the formation of the present Soufriere dome. This magmatic eruption is representative of the hazards caused by an explosive eruption of medium magnitude, although more intense eruptions have been identified in the last 10,000 years (Komorowski et al., 2005; Legendre, 2012). Recent studies suggest that a smaller magmatic eruption took place in 1657 (Legendre, 2012; Hincks et al., 2014).

Since that time the historical activity of La Soufrière has been characterized by persistent hydrothermal manifestations (fumaroles, solfataras, hot springs) culminating into intermittent non-magmatic steam-driven (phreatic) eruptions. Major phreatic eruptions occurred in in 1797–1798, 1797–1798, 1812, 1836–1837, 1976–1977, and minor ones in 1690 and 1956 (Lherminier, 1837a, 1837b, 1837c; Komorowski et al., 2005; Legendre, 2012; Hincks et al., 2014).

After the 1976-77 phreatic eruption (Feuillard et al., 1983; Komorowski et al., 2015 and references therein), the volcano remained in a state of repose notwithstanding low levels of fumarolic activity at the SW base of the dome, along the Ty fault (Zlotnicki et al., 1994; Allard et al., 1998; Komorowski et al., 2005; Villemant et al., 2005; Fig. 1) until 1992. Concomitant with the revival of shallow seismicity, degassing renewed on top of the lava dome in 1992, in parallel with re-activation of thermal springs that have remained dry since 1977 and the appearance of new ones at the southern base of the dome (Villemant et al., 2005, 2014). Fumarolic degassing was initially concentrated at the Cratère Sud (hereafter CS, Figs. 1,2), but gradually extended along the Napoleon fracture (1997) and to the Tarissan crater lake (1998). In 1998, the sudden onset of chlorine-enriched degassing from the CS fumaroles marked a significant change in the behaviour of the magmatic-hydrothermal system (Komorowski et al., 2001; Komorowski et al., 2005; Villemant et al., 2005, 2014). In parallel, boiling ponds of extremely acid water formed in 1997 at CS (mean pH of −0.1 and T°C = 88.8 ± 8.6 between 1998 and 2001; OVSG-IPGP data and Rosas-Carbajal et al., 2016), and since 2001 at the bottom of the Cratère Tarissan (mean pH of −0.2 in 2014) (Komorowski et al., 2005; Villemant et al., 2005; Komorowski et al., 2001; OVSG-IPGP, 1999-2019) (Figs. 1,2). Whereas the acid pond at the CS persisted for seven years, leaving place to an intense fumarolic degassing in 2003 (Komorowski et al., 2005), the acid thermal lake in the CratèreTarissan continued to be active until now (OVSG-IPGP, 1999-2019).

After 2007, fumarolic activity also propagated to Gouffre 56 (the explosion pit formed during the 1956 phreatic eruption, hereafter G56; Jolivet, 1958 and Figs. 1,2) then to the nearby Lacroix fracture (late 2011) and more eastward to the Breislack crater (2013, Figs. 1,2). The so-called Breislack fracture cutting the lava dome was involved in 4 of the 6 historical non-magmatic phreatic explosive eruptions of La Soufrière in 1797–1798, 1836–1837, 1956 (October), and 1976–1977 (eruption onset on 8 July 1976) (Komorowski et al., 2005, 2015; Rosas-Carbajal et al., 2016). The degassing area continued to expand on top of the lava dome, with the appearance of a new fumarole (Napoleon Nord, hereafter NAPN; Figs. 1,2) in July 2014, and of new vents (Napoleon Est 1 and Napoleon Est 2, hereafter NAPE1 and NAPE2) that opened further east (Figs. 1,2) between 8 and 10 February 2016 with a very small steam blast (in the sense of Mastin, 1995) with hot mud projections over a distance of 5–10 m radius.

The high concentration of hydrochloric and sulphuric acid plumes accompanied by high gas flows and a steady trade wind regime has destroyed the vegetation on the southwest flank of La Soufriere, contributing to small landslides of the degraded slopes, and to gas smell nuisances potentially harmful to people's health and felt since December 1997 by the population living downwind the volcanic plume (OVSG-IPGP, 1999-2019).

This reactivation ongoing since 1992 has required the implementation of an alert level scale set as of 1999 at the yellow level (i.e., vigilance), on a four-level scale (green, yellow, orange and red; OVSG-IPGP, 1999-2019). However, concern further increased recently owing to an accelerating unrest phase that developed in February–April 2018 and culminated with a magnitude 4.1 seismic activity peak, of same magnitude as the strongest earthquake recorded during the 1976–77 phreatic crisis (Feuillard et al., 1983).

In this study, we report and discuss the geophysical and geochemical features we observed to be associated with this recent peaking activity. Based on various data types, we attempt to interpret the triggering mechanism (magmatic versus hydrothermal) of this event and its significance within the unrest sequence initiated since 1992 at La Soufrière. Specifically, we try to decipher whether the observed phenomena may involve or not changes in a deep magmatic source and how unrest observables relate to the vigorous circulation and interaction of water, steam and hot gases in the porous and fractured host rocks.

## 3. Monitoring data: observations and preliminary assessments

In this section we present the data and observations resulting from our networks and measurements campaigns. A preliminary assessment is also given for each class of observation (seismic, geodetic, thermal, geochemical; see also Supplementary Table 1) with reference to the existing literature, in order to highlight the information to be extracted and then discussed quantitatively in Section 4.

*3.1. Seismic activity*

As mentioned above, after a brief repose period that followed the 1976–77 eruptive crisis, volcanic seismicity at La Soufrière renewed in 1992 (Fig. 3), concomitantly with the degassing unrest. Since then >14,000 earthquakes of volcanic origin were recorded (Fig. 3). Most of them were of low local magnitude $M_L$ (<1) and clustered in swarms lasting from a few days to a few weeks. Seventeen of all these volcanic earthquakes were strong enough to be felt locally, including five in 2013, one in 2014, and the most recent ones on 1 February, 16 April and 27 April 2018 (OVSG-IPGP, 1999-2019). After a relative minimum in both energy and number of events in 2016, the volcanic seismicity increased drastically since 2017 (Fig. 3). Compared to previous years, this increase can only partly be explained by improvements in the resolution of the seismic network. Thereafter, we describe the temporal and energy pattern of recent seismicity (from 1 st January 2017 to 30 July 2018). First of all, we list here the main features of observed waveforms (Fig. 4):

- volcano-tectonic (VT) signals, showing a high-frequency content (5–20 Hz) (Fig. 4a);
- long period (LP) signals, characterized by a low frequency (1–5 Hz), often appearing as nearly monochromatic signals (Fig. 4b) and associated with resonance phenomenon of the hydrothermal fluids in cracks (Ucciani, 2015);
- hybrid (HY) signals, showing the high-frequency content typical of VT events, most often at the beginning of the waveforms and accompanied by a low frequency content which often appears at the signal onset and is observed to the end of the event, in the signal coda (Ucciani, 2015; Fig. 4c);
- nested volcanic (VE) signals, appearing as small seismic packets in which events occur on the coda of the previous one (Fig. 4d), and which are not concomitant or precursor to a particular phenomenon. VE events differ from spasmodic burst defined in Hill et al. (1990) and consist in a sequence of several seismic events with very short inter-times, with very often >6 seismic events in a short sequence (~10s; Ucciani, 2015).

During 2017, the OVSG identified a total of 1432 volcanic earthquakes (Fig. 5a), all with local magnitude $M_L$ < 0.9, except for three events $M_L$ 1 -to 1.3 on 13 December. Seventy-two of the recorded events were of the LP type, whereas the majority (1360) were HY-type, with few VTs, and were similar to the seismic activity of dominantly volcanic origin observed in the previous years, implying a temporal continuity of seismic sources and processes (Ucciani, 2015; Ucciani et al., 2015). HY events are produced by fracturing and reservoir resonance phenomena related to the propagation of fluids. Some of these events (250 in 2017) are nested (VE-type), thus representing multiple closely-spaced ruptures within a patchy fractured medium. Given the superficial distribution of the hypocenters (mainly at depths between −0.8 km and 0.8 km below sea level – b.s.l.) (Figs. 5b,6a) such a low-energy micro-seismicity

attests to the vivacity of hydrothermal circulations within the shallow part of La Soufrière edifice (Ucciani, 2015; Ucciani et al., 2015; OVSG-IPGP, 2017). The 2017 activity released a total of 48.5 MJ of seismic energy (Fig. 5c).

The overall seismicity measured at La Soufrière in the first half of the year 2018 (Figs. 5a–c,6b) will be here discussed for four different relevant periods (January, February–March, April, May to July) that were chosen to provide a clear explanation of the sequence of observed key events, which are illustrated in Supplementary Figs. S1–S5. In January 2018, 78 earthquakes of volcanic origin were detected and located essentially under the dome of La Soufrière, at <0.5 km depth b.s.l., with the exception of an event (Fig. 5b, Supplementary Fig. S1). Most of them occurred concentrated in a swarm between January 2 and 5 (key event 1). The total energy released was about 3 MJ (Fig. 5c). A stronger seismic swarm of >30 earthquakes (key event 2) then succeeded on 1 st February 2018 between 12:55 local (16,55 UT) and 15:31 local. All hypocenters were located between 0.5 and 1 km b.s.l. (2 and 2.5 km deep under the dome summit) (Fig. 5b, Supplementary Fig. S2). The swarm started with events of very small magnitude but showed an increasing energy that ended with three earthquakes of magnitude ≥1.4, among which a felt one ($M_L$ 2.1, depth 1 km b.s.l., intensity III in the Saint-Claude commune (OVSG-IPGP, 2018a). The seismic energy released reached about 130 MJ (Fig. 5c). Between 2 February and 31 March the seismicity continued with 170 VT and hybrid-type earthquakes. An intensification of the activity can be observed since mid-March (Fig. 5a); Earthquakes were located under the dome of La Soufrière, at <0.5 km depth b.s.l.. (Fig. 5b), and of very low magnitude, releasing a total seismic energy of 14.7 MJ from 2 February to 31st March (Fig. 5c).

During April 2018, 545 volcanic earthquakes occurred beneath but also around the dome of La Soufrière, within a depth interval extending from −1 to 5.7 km b.s.l. The most prominent seismic activity concentrated in two swarms: on 16–17 April (key event 3: >140 VT and hybrid earthquakes in 48 h; Fig. 5a,b, Supplementary Fig. S3) and 27–28 April (key event 4: >180 earthquakes in 24 h; Supplementary Fig. S4). The first swarm was located under the SW base of the volcano (between −0.5 and 2.6 km b.s.l.). Twelve events had a magnitude ≥1.0 and hypocenters between 1 km and 1.6 km b.s.l. (or 2.5 to 3.1 km of depth below the summit). The main earthquake, at 18 h59 local on 17 April 2018 ($M_L$ 2.1 and depth 1.2 b.s.l.) was very slightly felt by the inhabitants of St Claude (weak macroseismic intensity, II; OVSG-IPGP, 2018b).

The second seismic swarm was instead located about 2 km north-northwest of La Soufrière summit dome. Two-thirds of the earthquakes occurred in the first two hours of activity and were of very small magnitude, with foci distributed between 1.0 and 3.1 km b.s.l. (or 2.5 to 4.6 km below the summit, Fig. 5b). However, at 20:15 (local) on 27 April a strong shock with $M_L$ 4.1 occurred, becoming the strongest volcanic earthquake recorded at La Soufrière for 42 years. Located 1.9 km below sea level, this earthquake was largely felt throughout Guadeloupe. In the nearest affected areas, a macroseismic intensity of V was estimated (OVSG-IPGP, 2018c). These two swarms in April 2018 released about 200 MJ and 90,000 MJ, respectively (Fig. 5c), the majority of which during the $M_L$ 4.1 earthquake on 27 April. Interestingly, the 27–28 April swarm is characterized by purely VT events, not showing any long-period coda (Fig. 4b). However, between 18 and 25 April, it was preceded by ~30 hybrid events that occurred in a zone surrounding the hypocentral region of the 16–17 April swarm.

During May, June and July 2018, 195 VT and particularly HY earthquakes of weak magnitude (≤1) occurred, beneath (between −1 and 2 km depth b.s.l.) and around the dome of La Soufrière (Fig. 5a,b, Supplementary Fig. S5). Seismic activity in May–July released 10 MJ of

---

**Fig. 1.** Map of the main structures, sites of historical eruptive activity and current hydrothermal activity of the La Soufrière dome (modified after Komorowski et al., 2005; Lesparre et al., 2012; and OVSG-IPGP, 1999-2019, with data taken from Hapel-Lachênaie et al., 1798; Peyssonnel and Maty, 1756; Lherminier, 1815; Lherminier, 1837a, 1837b, 1837c; Jolivet, 1958; Barrabé and Jolivet, 1958; Sheridan, 1980; Le Guern et al., 1980; Feuillard et al., 1983; Boudon et al., 1988; Komorowski et al., 2008; Nicollin et al., 2006; Feuillard, 2011; Brothelande et al., 2014; Hincks et al., 2014; Villemant et al., 2014, Allard et al., 2014; Rosas-Carbajal et al., 2016).
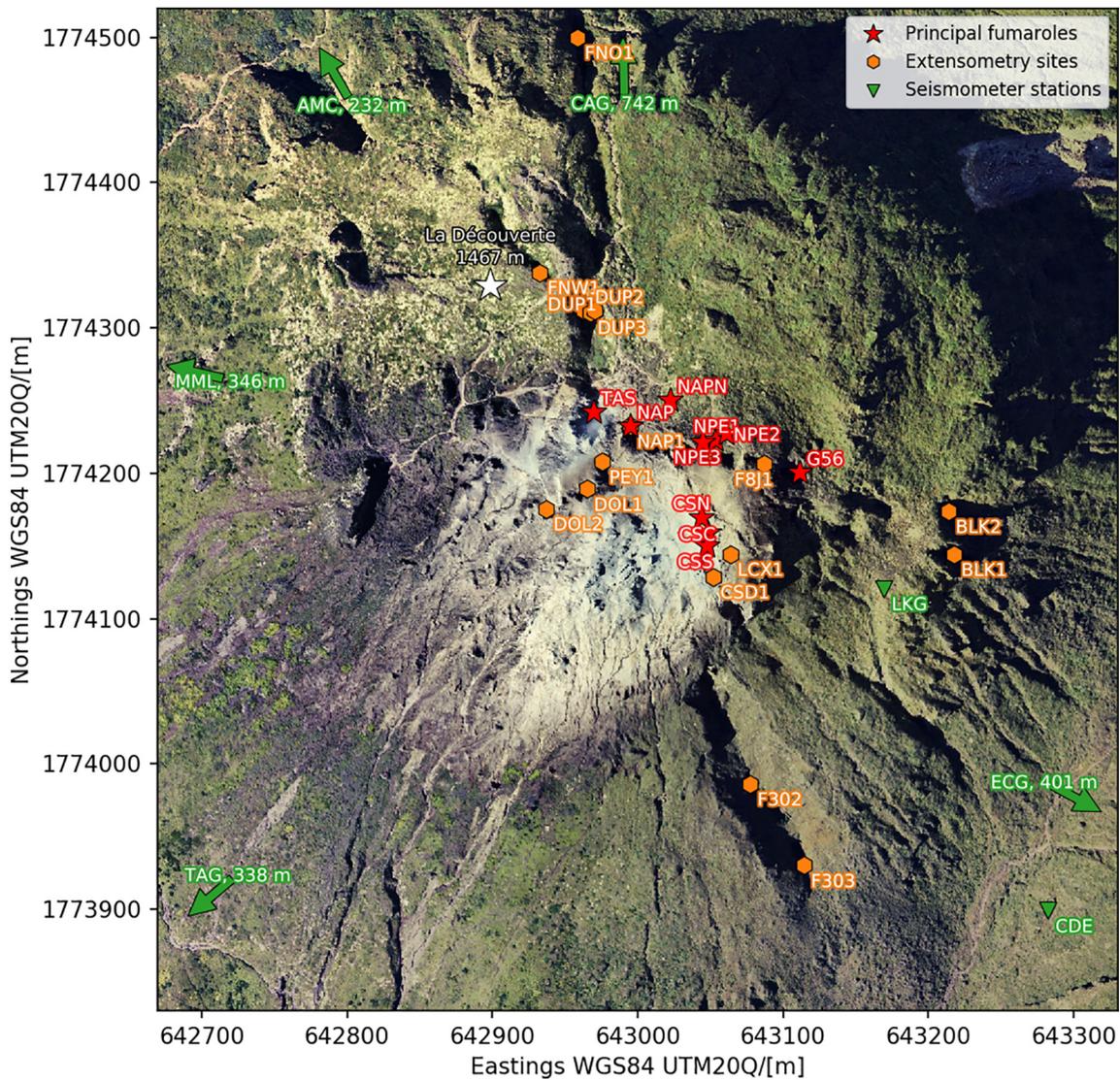
**Fig. 2.** Location of the principal fumaroles, extensometry sites and seismometer stations on the summit of La Soufrière. Site codes are as indicated in the text. The white star indicates the location of the highest point. Green arrows indicate directions to several volcanic seismometer stations which are off the current map view. The base image is a georectified orthophoto derived from aerial photographs acquired by Institut National de l'Information Géographique et Forestière (IGN) in 2010 . (For interpretation of the references to colour in this figure legend, the reader is referred to the web version of this article.)

seismic energy and marks a period of relative seismic calm after the highly energetic 27–28 April swarm.

### 3.2. Ground deformation

#### 3.2.1. GNSS data and patterns of deformation'

Fig. 7 presents the velocity field determined by Global Navigation Satellite System (GNSS) continuous and campaign measurements of La Soufrière network, with respect to the Guadeloupe archipelago. The network has evolved significantly since the first measurements in 1995 and the two first permanent stations in 2000 (HOUE and SOUF). The most important step occurred around 2015, with deployment of new permanent stations (CBE0, MAD0, PAR1, FNG0, AMC0, PSA1, TAR1) and more frequent reiteration campaigns. Therefore, velocity uncertainties depend mainly on the observation timespan and vary from <0.5 mm/yr for the oldest stations with about 20 years of data recording, to several mm/yr for stations installed recently. Stations located on the flanks of La Soufrière massif (HOUE, MAD0, CRB0, CBE0, FNG0, MAT0, and PAR1 in Fig. 7a) show velocities that vary from 0 to 1.5 mm/yr. The time series of these stations display remarkably steady state rate suggesting no significant variations of processes at depth during the

last twenty years. In particular, the general pattern of the deformation is not consistent with any inflation/deflation at depth.

To estimate the sensitivity of the network, we computed the Green's functions of a simple isotropic point source model using the varying-depth method to take the topography into account (Williams and Wadge, 1998) to determine the volume variations, $\Delta V$, in a 3-D grid (not shown) that can induce a maximum of 1 mm of displacement on the GNSS stations at the surface, considered here as an arbitrary threshold (de Chabalier et al., in preparation). For a source located at 10 km of depth below the dome, the detectability threshold of $\Delta V$ decreases from 800.000 m³ in 1995 to about 500.000 m³ after 2015. We also conclude that since 2015 the maximum depth of detection for a $\Delta V \approx 100.000$ m³ reaches 4–5 km. The deformation field of the flanks of the volcano does not reveal significant intrusion during the period of observation but we cannot exclude small intrusions, especially at depth larger than 6–7 km and in any case below the brittle-ductile transition. Nevertheless, the Basse-Terre deformation field can then be chosen as a reliable reference to determine the volcanic deformation of La Soufrière dome.

At the scale of the La Soufrière volcano, there is little deformation (<2 mm/yr on horizontal components) on the peripheral (>0.5 km)
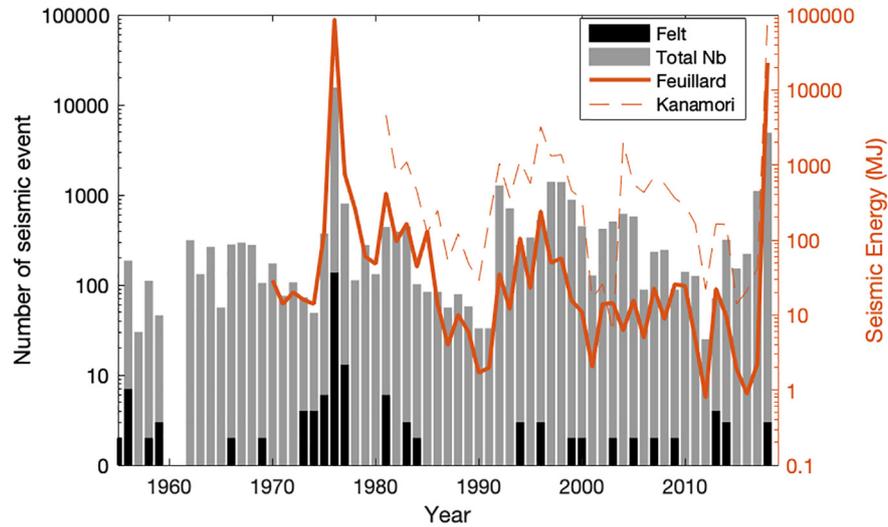
**Fig. 3.** Seismic activity of volcanic origin from 1955 to July 2018 (yearly histogram, with exception of 2018). Grey bars are the number of events per year. Black bars represent earthquakes felt by population. The two red lines indicate the released seismic energy, following Feuillard et al. (1983) (solid line) and Hanks and Kanamori (1979) (dashed line). The Feuillard et al. (1983) seismic energy is shown only for the purposes of continuity with the historical record. (For interpretation of the references to colour in this figure legend, the reader is referred to the web version of this article.)

sectors (NEZ2, AMC0, AMC1, RCB1, RCL2 in Fig. 7b), except in the south-western one. On the summit lava dome, the deformation signal is globally radial and reaches 3 to 7 mm/yr. Large displacement vectors (up to 9 mm/yr) towards the southwest point to a sliding zone downslope to the Bains Jaunes site, 1.3 km away from the top of the dome (Fig. 7).

In first approximation the horizontal components of GNSS velocities show that the pattern of the dome deformation is radial and centered on the Cratère Tarissan and Cratère Napoleon. Such a pattern, however, is disturbed by major faults and fractures crossing through the dome (North, Napoleon-Gouffre 56-Breislack system and the Dolomieu
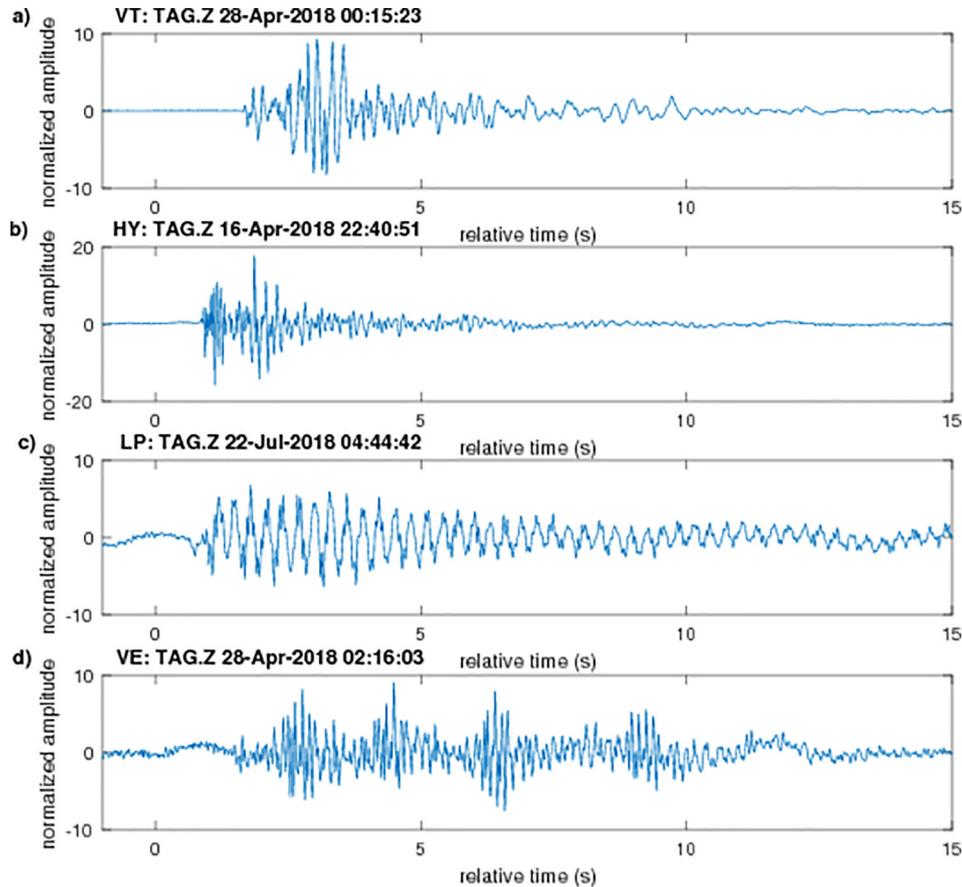


**Fig. 4.** Typical waveforms observed on the vertical component of TAG station, La Soufrière volcano. Panel a) "Pure" volcano-tectonic (VT) event. Panel b) Hybrid (HY) event (examples from shallow hydrothermal microseismicity and from ~2 km deep events recorded between the two subsequent swarms of April 2018). Panel c) example of "monochromatic" long-period (LP) event. Panel d) Nested (VE) event, typically of hybrid nature (examples from shallow hydrothermal microseismicity and from the 1 st February swarm). Note that VE events are observed by the OVSG since the 80's; because of the absence of a specific class in the literature, the observatory decided since the 90s to name these events as nested (*Volcaniques Emboités* in French).
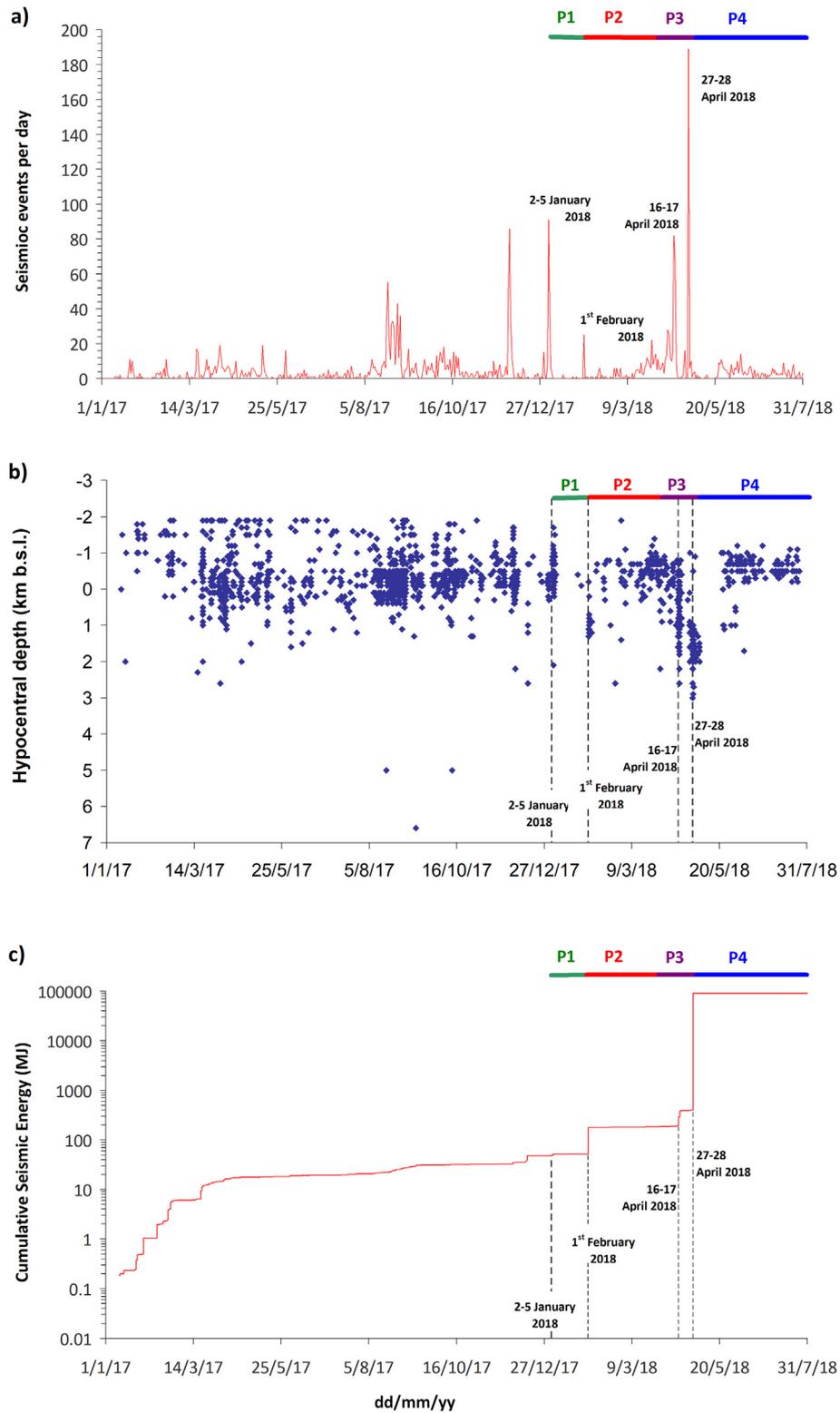
**Fig. 5.** Panel a) Seismic events observed on a daily basis from 1 st January 2017 to 31st July 2018. Panel b) Depths of hypocenters of seismic events observed from 1 st January 2017 to 31st July 2018, based on the adoption of the 1D velocity model of Dorel et al. (1979) and the use of the NonLinLoc algorithm (Lomax et al., 2000) for hypocentral location. Panel c) Semi-logarithmic diagram of cumulative (daily basis) seismic energy (Hanks and Kanamori, 1979) released by volcanic activity from 1 st January 2017 to 31st July 2017. Dashed lines mark the seismic swarms of 1 st February 2018, 16–17 April 2018 and 28–29 April 2018. The seismic energy release is dominated by the $M_L$ 4.1 event of 27 April 2018.

system, Fig. 1), resulting in three well identified blocks: a western block, an eastern block and a southern block (Fig. 7b). The aforementioned spreading to the south and southwest further superimposes on this pattern. The single exception in above pattern is the point ECH1, on top of a scoria cone (Fig. 7b), which slides downslope at a rate of 3.4 mm/yr to the north-northwest.

The thin orange zone in Fig. 7b highlights the dome sector where the strongest azimuthal direction gradients occur, together with important
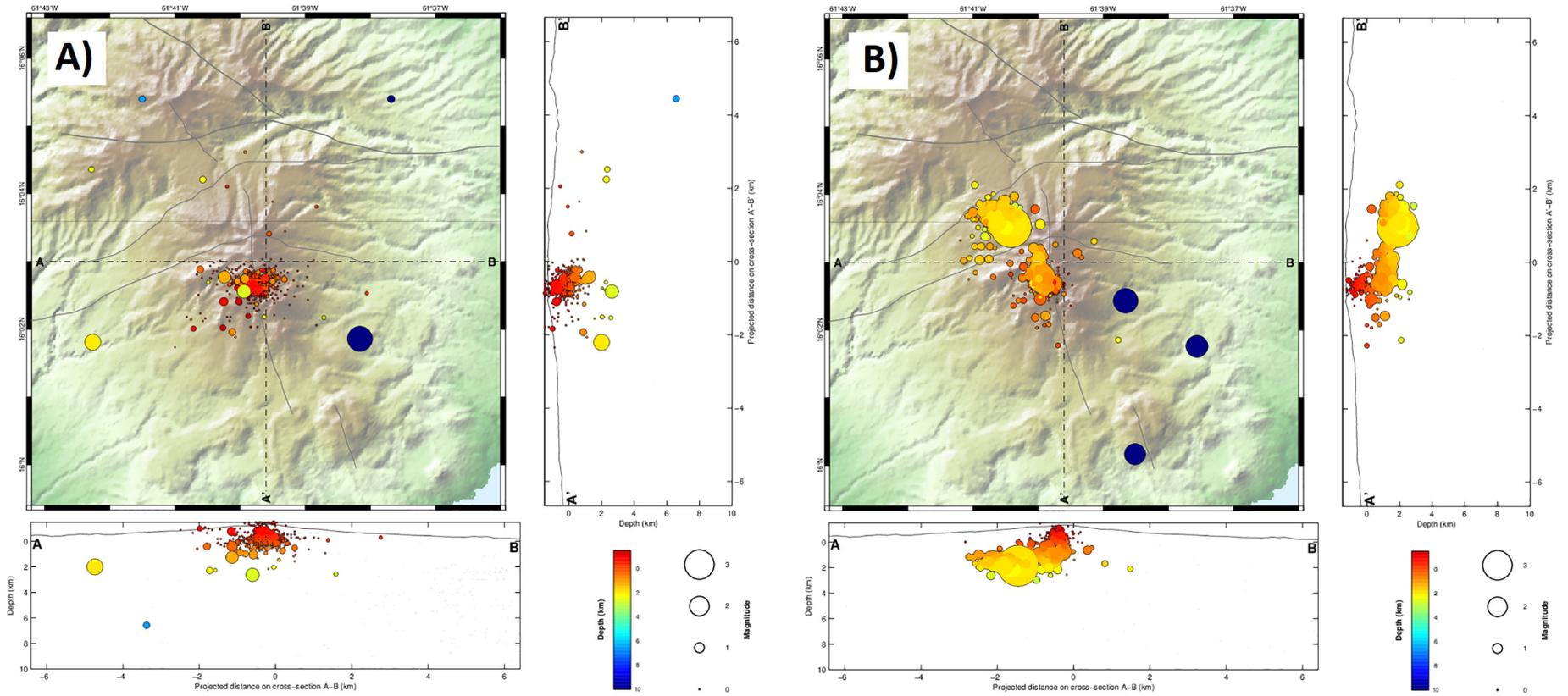
**Fig. 6.** Maps of the seismic activity recorded within, below and around the La Soufrière dome. Panel a) Seismic records in year 2017. Panel b) Seismic records from 1 st January 2018 to 31st July 2018. See Supplementary Figs. S1–S5 for relevant periods described in text. Blue circles refer to mid-crustal seismic (depth > 6 km b.s.l.) events which occurred off-volcanic axis and with maximum magnitude of 2.5. Results are based on the adoption of the 1D velocity model of Dorel et al., 1979 and the use of the NonLinLoc algorithm (Lomax et al., 2000) for hypocentral location. (For interpretation of the references to colour in this figure legend, the reader is referred to the web version of this article.)
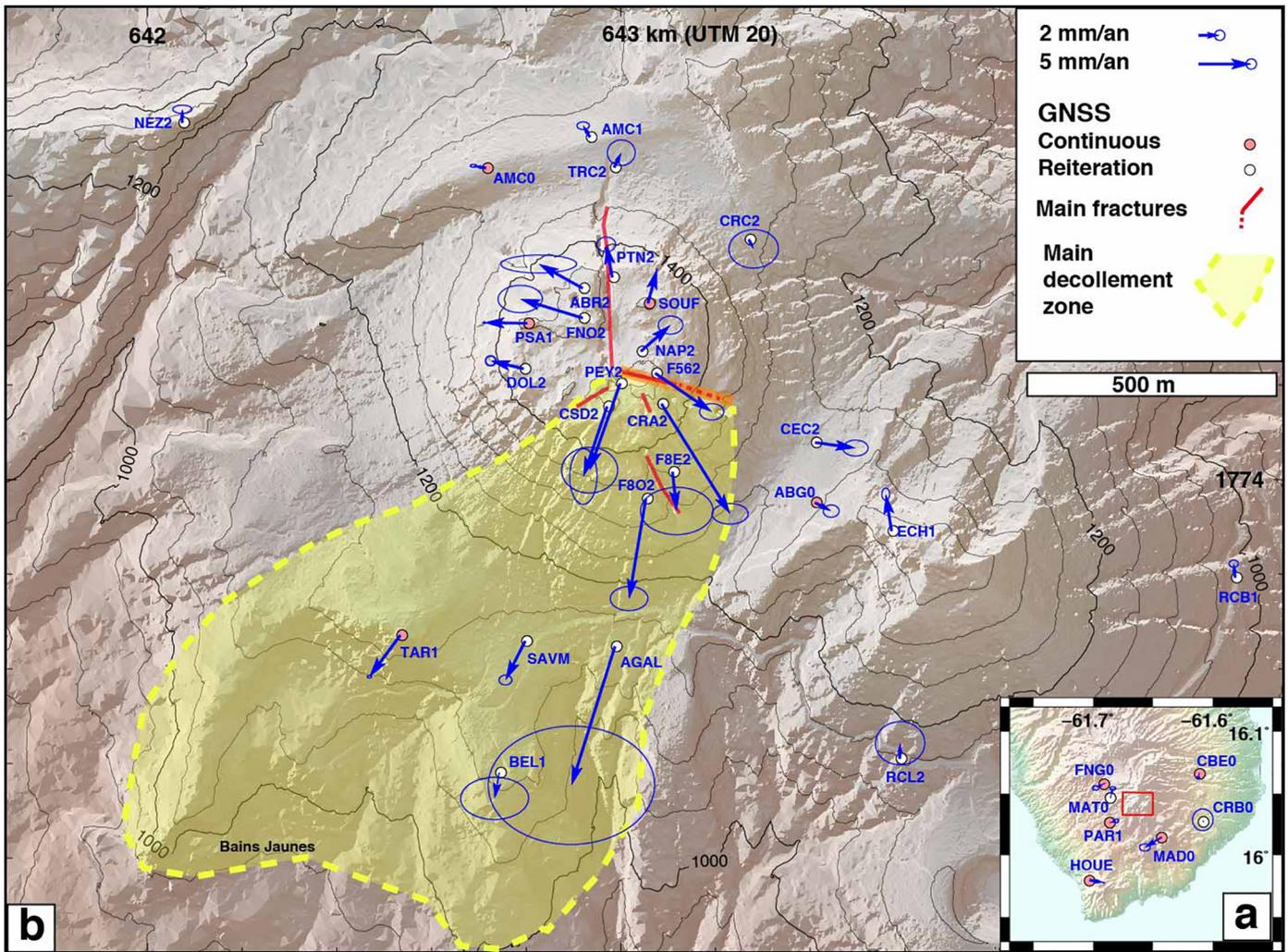
**Fig. 7.** GNSS horizontal velocities from 1995 to 2018 with respect to Guadeloupe archipelago (de Chabalier et al., in preparation). Error ellipses are 95% of confidence. The same scale have been used for south Basse-Terre Island (panel a) and La Soufrière volcano (panel b). Red box on panel a give location of panel b. (For interpretation of the references to colour in this figure legend, the reader is referred to the web version of this article.)

deformation. It corresponds to the Napoleon-Breislack fracture where fumaroles reactivated most recently between 2006 and 2014. This is the main extension zone whose opening reflects the combined effect of both hydrothermal flow (Rosas-Carbajal et al., 2016) and the southwest flank sliding of the dome. The other gradient zones (yellow-dashed in Fig. 7b) are scarcely or not at all marked by fumarolic activity and fracturing, but in some sectors are characterized by diffuse soil degassing (Allard et al., 1998; Komorowski et al., 2013; Fig. 1).

### 3.2.2. Extensometry

One-dimensional extensometry measurements are taken on fractures 0.4 to 20 m wide. Since the installation of the extensometry network in 1995, measurements showed a general tendency of opening of the faults and fractures in the active fumarolic zones, as well as along the dome fracture that formed during the phreatic eruption of 30 August 1976. Gouffre Napoleon (NAP1 in Fig. 8) is the site affected by the largest extension and shows that extensional movements occurred with different rates in different periods (Fig. 8b). Specifically, we recognize four consecutive periods (1995–1999, 1999–2003, 2003–2016, 2016-to date), the second marked by quiescence and the others by extension, with the most recent period characterized by the largest extension rate.

In general, fracture opening at some sites appears to be partially compensated by local closing of other, adjacent, fractures located outside or on the margins of the active fumarolic zone. This behaviour strongly suggests that the shallow stress field is determined at the depth of the hydrothermal system by a mechanism similar to simple shear (Buck et al., 1988). The opening trend at almost all fractures observed since mid-2016 is thus compatible with a pressure increase in the hydrothermal source, determining the displacement field and the switch to conditions close to pure shear (Buck et al., 1988).

Interestingly, a closer inspection of data between 9 March and 25 April 2018 shows a reversal in this opening trend (Fig. 8a), implying a slight closure of the active fumarolic zones on the top of the dome except for one point along Gouffre Dupuy (DUP1, Fig. 8a). Such a reversal thus indicates a hydrothermal pressure drop. Instead, subsequent measurements in June and August 2018 reveal a renewal of the generalized extensional trend (Fig. 8a), suggesting a new overpressure phase of the hydrothermal source of deformation.

### 3.3. Fumarole thermal data

CS fumaroles (CSS, CSC, CSN; Fig. 2) show generally high flow rates and large deposits of solid sulphur. A decrease in the discharges was observed after the passage of hurricane Maria (mid-September 2017), probably in response to the huge amount of water infiltrated into the subsoil and thus into the shallow hydrothermal system (the measured rain water level on top of the dome was 440 mm in 24 h due to the
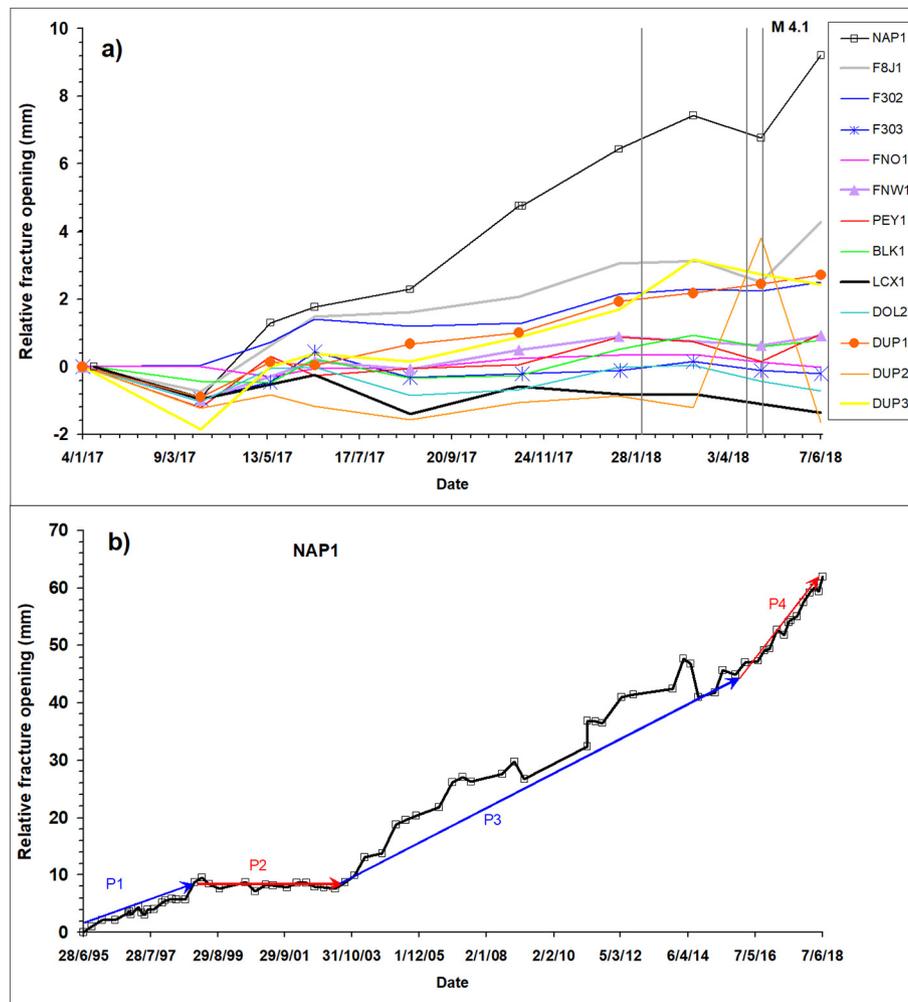
**Fig. 8.** Panel a) Extensometric measurements during the last year (August 2017–July 2018) at all sites. Note the enhanced dynamics shown by the NAP1 site. Panel b) Extensometric measurements at the NAP1 site since network installation (1995) with indication of the four periods, corresponding to different extensional velocities (see text). See Fig. 2 for location of measurement sites.

hurricane's passage, 2017; OVSG-IPGP, 2017). Starting in November 2017 fumarole fluxes have begun to increase to pre-hurricane values.

Driven by the interaction between hot magmatic fluids and the hydrothermal system, La Soufrière manifestations develop a number of sites where heat is preferentially transported to the surface, as commonly observed at many volcanoes in hydrothermal stage (e.g. Chiodini et al., 2001; Harris, 2013; Sigurdsson et al., 2015). Convection of water vapour transports heat from depth to the surface. Vapour travelling through the most porous conduits leads to fumaroles (e.g. CS). Near-surface steam condensation leads to large temperature gradients, conduction of heat to the surface forming thermal anomalies (e.g. Faille de la Ty, FTY; Fig. 1). Condensed water escapes laterally, mixing with meteoric water and forming hot springs. At La Soufrière the latter contribute marginally to the overall heat budget (Allard et al., 2014; Gaudin et al., 2016) and we will not discuss them further. Moreover their chemistry and temperature have remained stable over the last 10 years (Villemant et al., 2005, 2014; Ruzié et al., 2012, 2013; OVSG-IPGP, 1999-2019). Accordingly, thermal monitoring in the form of (discrete) manual temperature measurements have been carried out over the last 20 years, roughly one per month. More recently, continuous measurement stations utilising PT100/PT1000 resistance temperature detectors have been installed at several key fumarolic sites with acquisition rates of 1 s. At the time of the 2018 crisis, the CS fumaroles (central, north and south, labelled CSC, CSN, CSS, respectively; see Fig. 2 for

location) had been instrumented with continuous measurements commencing on 14 April, and were routinely measured manually (for CSC, CSN and NAPN). Additionally, vent speed measurements were made using a Pitot tube instrument at CSC, CSN, CSS and NAPN though, especially in the case of CSS which requires specialised roped-access techniques, these were done less frequently.

The historical temperature record shows that fumarolic vents typically have temperatures corresponding to saturated steam vapour at the pressure of the summit (~95 °C) (Fig. 9a). Fumaroles CSC and CSN have shown short-lived fluctuations up to 140 °C (cf. June-1999 to Feb-2000 at CSN) and longer-duration increases up to 110 or 120 °C (cf. Sept-2011 to Mar-2013 at CSC). Early during the April-2018 unrest phase, the fumarole temperatures rose again, attaining maxima of 111.4 °C at CSC on 3rd April, and 109.7 °C at CSN on 23rd March (according to the manual measurements). We also note the remarkably constant temperature at NAPN at around 95 °C since its appearance in 2014 (Fig. 9b). After the aforementioned maxima, temperatures dropped rapidly to 104 °C (19 April 2018) and then to the background saturated vapour value (96 °C, 28 April 2018). The rapid temperature drop in the CS area is well detailed by the continuous measurements at CSC and CSN (Fig. 9b) which demonstrates that the saturated steam temperature was reached on 26 April, one day prior the $M_L$ 4.1 earthquake. Indeed, the continuous measurements indicate that the temperature decreased in several stages, the temperature decreasing by 2–4 °C
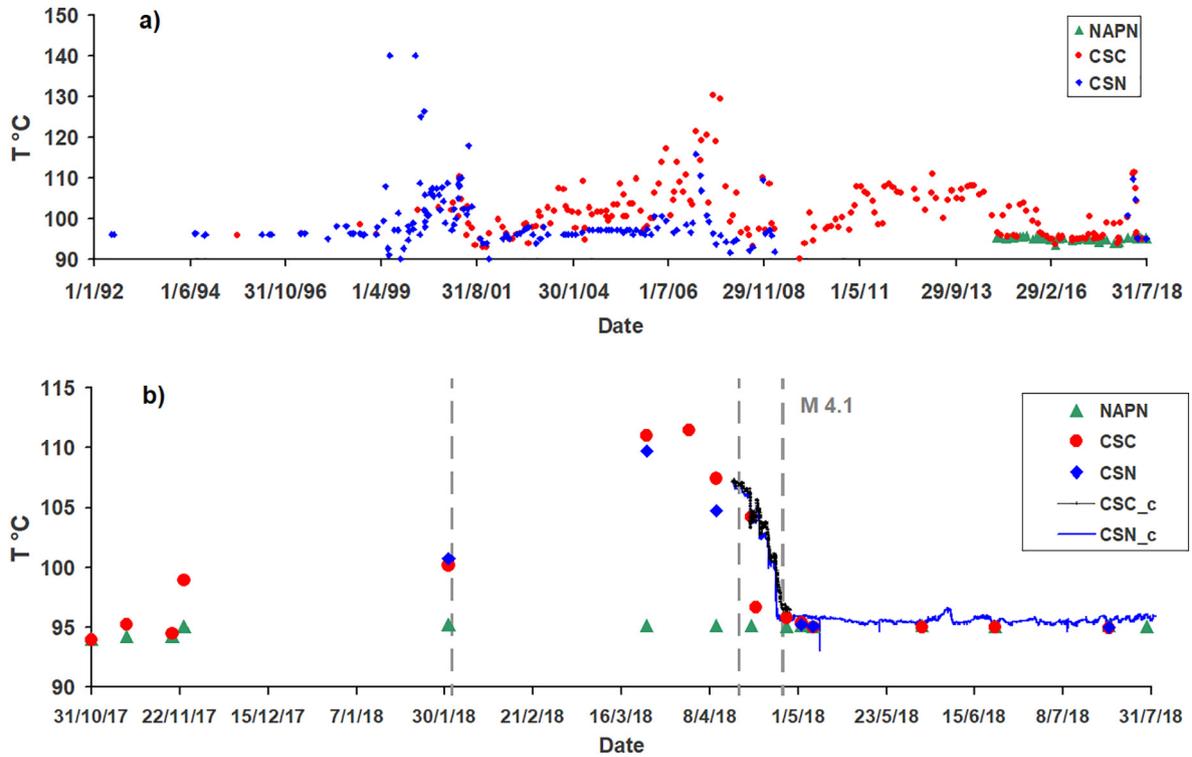
Fig. 9. Panel a) Temperatures (discrete measurements) at CSC, CSN and NAPN fumarolic sites over the last 26 years. Panel b) Temperatures since October 2017; symbols refer to discrete measurements at fumarolic sites, the solid lines refer to continuous measurements at the CSN and CSC (CSN_c and CSC_c, respectively) since installation in April 2018. Vertical lines correspond to the onset of the three major seismic swarms of 2018 (1st February, 16 April and 27 April).

at each stage. From these data, we conclude that during the early 2018 unrest phase, fumarolic fluid at CS was superheated with respect to the temperature of boiling water at the elevation (Fig. 9).

In parallel, venting gas speeds measured at CSC and CSN dropped from 80 and 53 m/s, respectively on 6th April to 20 and 33 m/s, respectively, on 25th April. Following the $M_L$ 4.1 earthquake fumarolic flow rates decreased, becoming so low that, on 29th April, it was not possible to reliably measure gas speeds from vents located at any of the CS vents. Fumarole heat flux, which is globally proportional to vent speed, thus also decreased by a factor of four from around $20.0 \pm 4.5$ MW to around $5.0 \pm 1.1$ MW (see Fig. 10; for details of these calculations, please refer to Supplementary Material). These vent speeds and the temperature measurements noted above suggest that the total steam flux at CS dropped from a maximum of around $8.0 \pm 1.0$ kg/s at the beginning of April to about $3.5 \pm 0.5$ kg/s soon after the 27 April. This latter

value is of same order as CS steam fluxes previously estimated from MultiGAS traverses in 2006 (0.87 kg/s), 2012 (1.72 kg/s) and May 2016 (0.52 kg/s) (Allard et al., 2014; Tamburello et al., 2019), indicating a slow but significant over the past decade or so. Instead, our values of steam and enthalpy flux are substantially lower than those of Gaudin et al. (2016), who estimated the CS steam and enthalpy fluxes (thermal camera data collected in 2010) to be $19.5 \pm 4.0$ kg/s and $48.0 \pm 9.8$ MW, respectively. We note that Gaudin et al. (2016) estimated the fluxes at some distance from the vent and did not correct for the effect of entrainment of ambient air into the plume and the resulting increase in plume volume. As such, it is peculiar, even given the fluctuating though increasing activity at La Soufrière, that the 2010 survey found such large values for both steam and enthalpy flux, particularly with respect to the 2006 and 2012 MultiGas-based estimation. It may be the case that the approximations made during their study affected their results
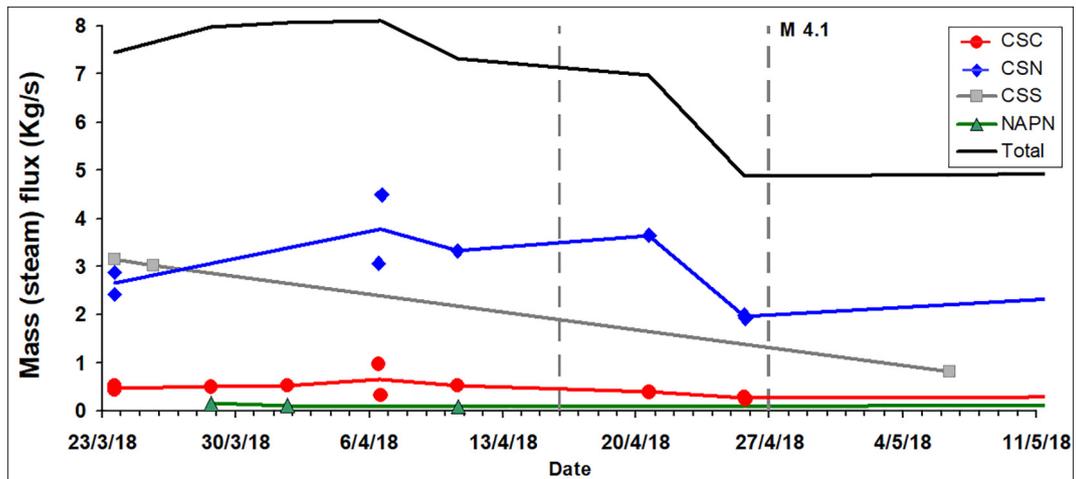


Fig. 10. Steam fluxes determined from gas exit velocities (measured by Pitot tube) from 23 March 2018 to mid-May 2017.

more than was anticipated, potentially doubling the measurement uncertainty, in which case their values fall more in line with those found here. A complete inventory of the heat flux discharged by the dome (particularly its partitioning between fumarolic, soil diffuse and hot spring fluxes) is currently missing. Its temporal evolution since the 2010 estimate (Gaudin et al., 2016) is thus uncertain. However, we must suspect a thermal flux increase since 2010, because of the reactivation of many emission sites (e.g., G56, Lacroix Superieur, NAP; see below), the emergence of new sites (NAPN, NAPE1, NAPE2) and the concurrent increases in soil temperatures and extent of vegetation decay in soils with degassing at the summit (OVSG bulletins).

### 3.4. Fluid Geochemistry

#### 3.4.1. Fumarole chemistry

For fumarolic sampling and gas analysis at La Soufrière the OVSG-IPGP Observatory uses the "Giggenbach"-type soda bottle methodology (e.g., Giggenbach and Goguel, 1989; see Supplementary Material). This method permits to obtain the complete, internally consistent, chemical composition of the fumarolic fluid, with an accuracy and precision that could not be attained by previous chemical routines, essentially based on $P_2O_5$–filled sampling bottles (Fabre and Chaigneau, 1960). The reader may refer to Allard et al. (2014) and particularly to Villemant et al. (2014) for the database of gas samples obtained with this latter sampling technique. Since November 2017, the procedures for gas sampling and analysis were improved at OVSG-IPGP. For consistency, we here report and discuss only the data obtained from that date. Fig. 11 shows the temporal evolution of major chemical indicators (molar ratios for gas/steam, C/S, $CO_2/CH_4$, $He/CH_4$, $H_2/H_2O$ and $CO/CO_2$) in the CSC fumarole, the most accessible and surveyed fumarole on top of La Soufrière (see Table 1 for chemical analyses). For comparative thermodynamic calculations (see Section 4.2), we also include the other available and fully consistent soda-based data from summit emissions, sampled in 1997 by Brombach et al. (2000) and in July 1976 by Chevrier et al. (1976).

Since water vapour in La Soufrière fumaroles is essentially of meteoric (rainwater) origin whereas the major gas components have a magmatic derivation (Brombach et al., 2000; Villemant et al., 2014; Allard et al., 2014), variations of gas/steam ratio essentially reflect changes in the proportion of the deep, magma-derived, gas with respect to the meteoric component in the hydrothermal system. This ratio can increase due to either the arrival of magmatic gases or/and the condensation of water vapour. Instead, increased boiling will make it decreasing because of steam addition. As regards the C/S ratio, it can increase either due to either the uprise of deep magmatic gas (often associated with a temperature increase), because $CO_2$ in magmas is much less soluble than sulphur-bearing gas species and then degasses much earlier (e.g., Moretti et al., 2003 and reference therein) or a loss of sulphur in the hydrothermal system (scrubbing of $SO_2$ and $H_2S$, as well as precipitation of sulfides and/or native sulphur; Allard et al., 2014; Villemant et al., 2005; Tamburello et al., 2019),this latter process being often associated with a decrease in temperature.

Methane is absent in hot magmatic gases and is a typical component of low-temperature or/and reduced hydrothermal fluids (Giggenbach, 1987). The $CO_2/CH_4$ ratio is thus a powerful indicator of magma degassing episodes because it is orders of magnitude higher in magmatic gases than in hydrothermal fluids. Accordingly, an increase of $CO_2/CH_4$ in fumaroles clearly indicates an enhanced supply of $CO_2$-rich oxidized and hot magmatic gas whose effect will be to oxidize and potentially warm the base of the hydrothermal system, thereby limiting the conversion of $CO_2$ in $CH_4$ at low temperature (Chiodini, 2009). Depending on the extension of the hydrothermal system and the intensity of the magmatic gas injection, there may be a time delay between the gas arrival and the observation of a $CO_2/CH_4$ peak anomaly at the surface (Chiodini, 2009).

Similarly, peak increases of the $He/CH_4$ ratio point to the arrival of deeply derived gases of either magmatic (e.g., Chiodini et al., 2015) or crustal origin, which can be discriminated on basis of the $^3He/^4He$ isotopic ratio. At La Soufrière, helium present in both fumaroles and hot springs has been shown to be of pure MORB-type magmatic origin (e.g. Allard, 1983; Ruzié et al., 2012, 2013; Jean-Baptiste et al., 2014). Owing to their much lower mass than $CO_2$, both $^3He$ and $^4He$ can diffuse much faster than $CO_2$ over the ascent path of fluids, so that deep gas inputs into a hydrothermal system should be first detected by increasing $He/CH_4$ and later on by increasing $CO_2/CH_4$.

CO and $H_2$ are fast reactive species obeying the following equilibria.

$$CO + 1/2O_2 \Longleftrightarrow CO_2 \tag{1}$$

$$H_2 + 1/2O_2 \Longleftrightarrow H_2O \tag{2}$$
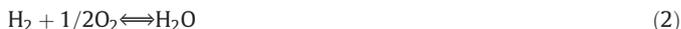
Owing to the fast kinetics of these two reactions, both the $CO/CO_2$ and $H_2/H_2O$ ratios are isensitive indicators of late-stage gas reequilibration upon ascent and changing oxidation environment ($fO_2$). Increasing $fO_2$, at a given T, favors the oxidized molecule (either $H_2O$ or $CO_2$). The geothermal literature has shown that along typical unspecified hydrothermal mineral buffers of the type $logfO_2 = a − b / T$ (K) (with $a$ and $b$ being positive constants) both $H_2/H_2O$ and $CO/CO_2$ ratios increase with increasing T, hence $fO_2$ (e.g., D'Amore and Panichi, 1980; Giggenbach, 1980; Chiodini and Marini, 1998). In addition, $H_2/H_2O$ values can also reflect the occurrence of secondary phenomena, such as boiling and steam condensation from separated and equilibrated single vapours (Chiodini and Marini, 1998; Brombach et al., 2000; see also Section 4.2). On the other hand, the $CO/CO_2$ ratio is not affected by secondary effects, so that its increase is more directly associated to the heating of the hydrothermal system (Chiodini and Marini, 1998; Chiodini et al., 2015). It is worth recalling that coexistence of water vapour and the liquid (boiling pure water or brines) implies that heating and pressurization are associated, determining the joint increase of both temperature and pressure fixed along the liquid-gas univariant equilibrium.

We note that the gas/steam ratio did not change appreciably in concomitance with seismic swarms, though it did increase by a factor of four (Fig. 11a) on 2 June, before rapidly returning to previous value on 21 June. The present-day gas/steam ratios, except the peak values, are in line with those measured in 1997 (Brombach et al., 2000) and also 1976 (Chevrier et al., 1976). The C/S ratio fluctuates around a mean value of 4 (Fig. 11b), within the range of 1976 values (Chevrier et al., 1976). This is however well below the 1997 data, that were recorded after the dome summit re-activation, when the "dry" gas was essentially made of $CO_2$ (Brombach et al., 2000), prior to the sulphur enrichment and the appearance of HCl in 1998 (Komorowski et al., 2005; Villemant et al., 2014). No change of the C/S ratio is recorded before, during or after the seismic swarms. The rise in the $CO_2/CH_4$ ratio (Fig. 11c) appears to occur gradually throughout the period of observation (from 100,000 in November 2017 to 150,000 on 30 July 2018) and is characterized by an increase on late April, followed by a peak at 260000 on 2 June. We note also that Brombach et al. (2000) did not report $CH_4$ emanating from the summit fumaroles in 1997, which suggests that the activity of the summit hydrothermal system was at its early stage, developing under the forcing of deep magmatic gases.

The behaviour of gas/steam and $CO_2/CH_4$ indicators is likely related to the increasing influx of a deep gas component, heavily discharged at the surface on 2 June, and bearing a magmatic signature particularly evidenced by the $CO_2/CH_4$ ratio. Nevertheless, we cannot exclude that secondary effects such as steam condensation upon cooling, and the consequent scrubbing of soluble components, play a role in determining the observed values, especially for sulphur species and so the C/S ratio. This effect is well known to have been important at La Soufrière de Guadeloupe (Brombach et al., 2000), and has certainly contributed to the development of the shallow hydrothermal system. However, its role is
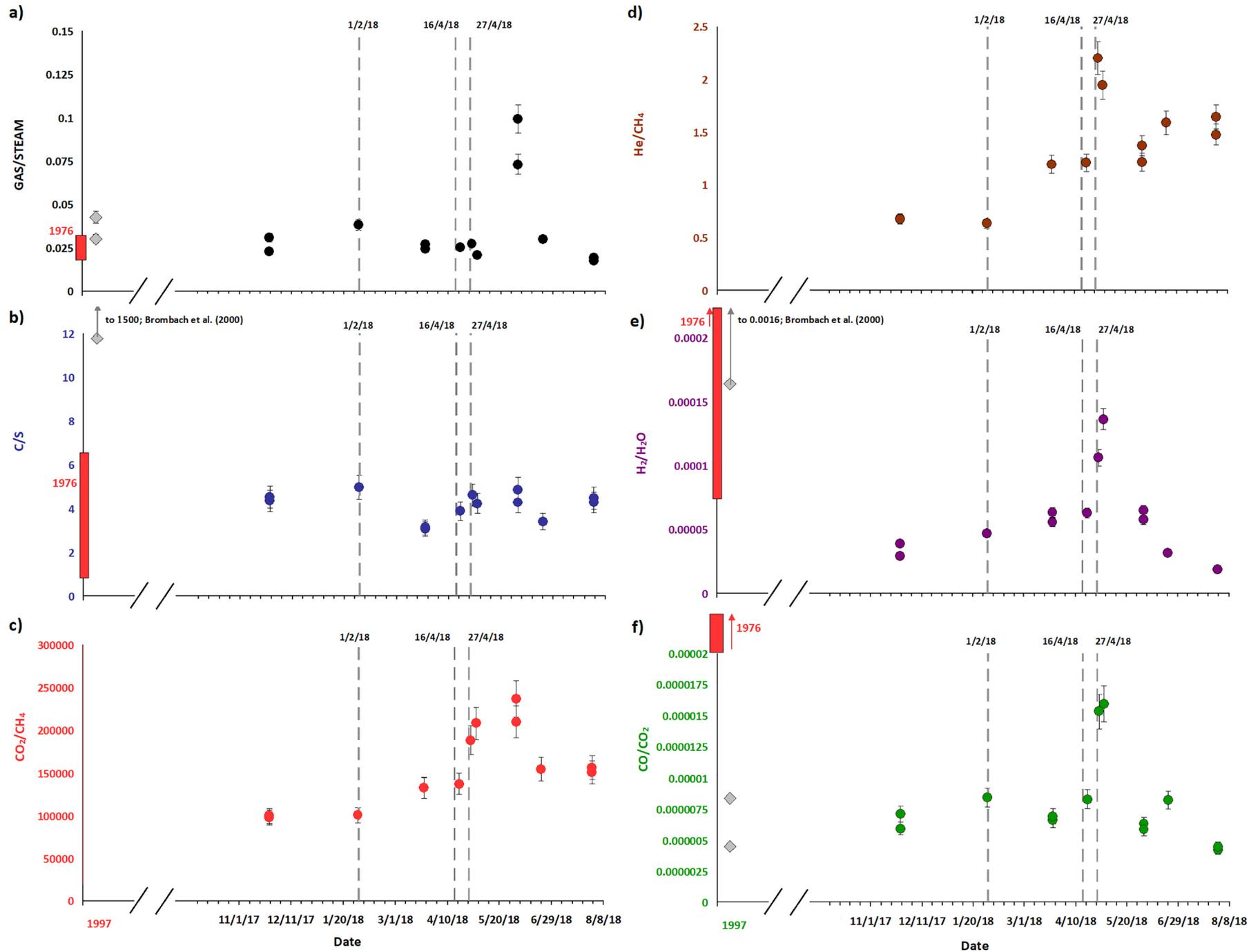
**Fig. 11.** Molar ratios of relevant chemical species at CSC fumarole since November 2017. Also shown are data from the 1997 sampling in Brombach et al. (2000). Left-side diagrams (panels a–c) show maxima on 2 June 2018, associated with the arrival of the most magmatic gas composition. Right-side diagrams (panels d–f) show maxima on 28 April 2018, revealing a peak in hydrothermal pressure and temperature related with the onset of the M 4.1 earthquake on 27 April 2018. Due to the very low flux at CSC, on 2nd May sampling was carried out at the nearby "twin" CSN fumarole. Vertical lines refer to the 2018 seismic swarms. Error bars are ±11%, or within symbol size if not shown. See Table 1 for errors on concentration measurements and the Supplementary Material for additional details.

**Table 1**

Chemical analyses of fumarolic gases from Cratère Sud Central (CSC) fumarole. Note that the 2 May sample was taken at the Cratère Sud Nord (CSN) fumarole, which is conjugated to the CSC one. Errors on concentrations are given beneath the name of each gas species in the table heading. See Supplementary Material for details.

| Date | Fumarole | $H_2O$ | $CO_2$ | $H_2S$ | $H_2$ | $CH_4$ | CO | $N_2$ | He | Ar | $O_2$ |
|------|----------|--------|--------|--------|-------|--------|-----|-------|-----|-----|-------|
|      |          | ±2%    | ±8%    | ±7%    | ±5.4% | ±4.5%  | ±4% | ±2%   | ±5.5% | ±12.5% | ±58% |
| 30/07/2018 | CSC | 981,210 | 15,283 | 3412 | 18 | 0.10 | 0.06 | 75 | 0.14 | 0.34 | 0.06 |
| 30/07/2018 | CSC | 982,650 | 13,983 | 3274 | 18 | 0.09 | 0.06 | 74 | 0.15 | 0.35 | 0.05 |
| 21/06/2018 | CSC | 970,960 | 22,321 | 6574 | 30 | 0.14 | 0.18 | 112 | 0.23 | 0.59 | 0.43 |
| 02/06/2018 | CSC | 931,921 | 54,947 | 12,830 | 54 | 0.26 | 0.35 | 245 | 0.36 | 2.07 | 0.29 |
| 02/06/2018 | CSC | 909,747 | 74,557 | 15,305 | 59 | 0.32 | 0.44 | 313 | 0.38 | 3.07 | 14.11 |
| 02/05/2018 | CSN | 979,901 | 15,990 | 3777 | 134 | 0.08 | 0.26 | 195 | 0.15 | 2.38 | 1.05 |
| 28/04/2018 | CSC | 973,404 | 21,630 | 4695 | 103 | 0.12 | 0.33 | 165 | 0.25 | 1.50 | 0.60 |
| 19/04/2018 | CSC | 975,536 | 19,334 | 4982 | 61 | 0.14 | 0.16 | 85 | 0.17 | 0.49 | 0.76 |
| 23/03/2018 | CSC | 973,775 | 19,639 | 6427 | 62 | 0.15 | 0.13 | 94 | 0.18 | 0.73 | 2.04 |
| 23/03/2018 | CSC | 976,232 | 17,878 | 5706 | 54 | 0.13 | 0.12 | 127 | 0.16 | 1.25 | 0.69 |
| 31/01/2018 | CSC | 963,147 | 30,514 | 6139 | 45 | 0.30 | 0.26 | 153 | 0.19 | 1.39 | 0.39 |
| 24/11/2017 | CSC | 977,581 | 18,134 | 4171 | 28 | 0.18 | 0.11 | 85 | 0.12 | 0.35 | 0.09 |
| 24/11/2017 | CSC | 969,947 | 24,491 | 5402 | 37 | 0.25 | 0.17 | 120 | 0.17 | 0.79 | 0.75 |

presently subordinate and the chemical variations shown by the hydrothermal fluids are dominated by primary compositional variations due to degassing of the source. This is in fact well testified by 2 June samples, for which steam condensation cannot explain why they also have the largest $CO_2/CH_4$ value, given the much larger solubility of $CO_2$ with respect to $CH_4$ in condensed steam (Giggenbach, 1980).

These elements, along with the temperature increase, confirm that the hydrothermal system was infiltrated by a major pulse of deep gas. This pulse determined also the rise in $He/CH_4$, $H_2/H_2O$, and $CO/CO_2$ ratios, all peaking around 28 April and 2 May (Fig. 11d–f). The $He/CH_4$ ratio (Fig. 11d) increases between November 2017 and late July 2018 by a factor of three, showing the increasing contribution of a deep gas, likely of magmatic origin (e.g., Chiodini et al., 2015). A sharp peak in $He/CH_4$ is observed on 28 April 2018, right after the $M_L$ 4.1 earthquake, which anticipates any other peak, including the $CO_2/CH_4$ peak (Fig. 11c). Both $H_2/H_2O$ and $CO/CO_2$ show sharp peaks on 2 May(0.00013 and 0.000015, respectively; Fig. 11e) consistent with the onset of more oxidized conditions and the heating up of the hydrothermal system upon the arrival of hot and oxidized deep gases (e.g., Chiodini and Marini, 1998). Contrary to the $He/CH_4$ ratio, both ratios do not show an increasing baseline, as shown by the fact that after the peak phase the both attained their lowest values on 30 July 2018. $H_2/H_2O$ peak values overlap with 1976 (Chevrier et al., 1976) values but plot below 1997 data, which were much higher than those observed nowadays because of important steam condensation (Brombach et al., 2000). On the contrary, $CO/CO_2$ values compare very well with 1997 data but are much lower than those of 1976, suggesting that 2018 heat inputs are below those involved in the 1976 phreatic eruption.

### 3.4.2. MultiGAS measurements

The OVSG-IPGP uses routinely a portable MultiGAS station (Aiuppa et al., 2005; Shinohara, 2005) to measure the concentration of gas emitted by major craters and structures, and also perform gas flux measurements along traverses through main fumarole plumes (e.g., Allard et al., 2014; Tamburello et al., 2019).

From 2012 to 2016, gas fluxes increased by a factor ~3 and ~2 at CS and Tarissan, respectively, while gas fluxes from G56 have varied from below detection limit to values that are comparable to those from Tarissan (e.g., Allard et al., 2014; Tamburello et al., 2019). Since 2016, measurements show constant gas fluxes at Tarissan and South Crater, with mean values of 5.7 (± 1.6) and 7.5 (± 1) t/d, respectively. Taking into account the high error (~40%) on the flux determination (Tamburello et al., 2019), the gas fluxes at Gouffre 56 can be also considered constant, despite a noticeable variability (4.7 ± 2.6 t/d). Gas concentrations measured on the dome (Fig. 12a) show that a strong chemical perturbation started in March 2018, characterized by increasing $CO_2/H_2S$ and $SO_2/H_2S$ ratios. In details, the C/S ratio is constant at Cratère Sud, as observed with the Giggenbach bottle. The average C/S

value returned by MultiGAS is however ~2 (Fig. 12a), instead of 4 for the data from Giggenbach bottles (Fig. 11). From March 2018, the C/S MultiGAS ratio increased at Tarissan and Napoléon Nord, but not at Cratère Sud and G56. At the same time, the $SO_2/H_2S$ ratio increased slightly at Napoléon Nord and significantly at Cratère Sud reaching a maximum value of 0.18 (Fig. 12b). This is the highest $SO_2/H_2S$ ratio, by at least a factor 2, measured at La Soufrière since the start of MultiGAS measurements in 2012. After 2 May 2018, this ratio returned to previous values, even below detection limit. Furthermore, a MultiGAS survey was also carried out between 16 and 23 March 2018 in the surroundings of the NAPN vent, at a site around twenty meters away from the NAPN vent (Fig. 2b) that does not show a proper fumarolic activity (i.e. a visible flux of steam) but was reactivated with a dry gas emission. Measurements yielded values up up to T = 94 °C, $SO_2/H_2S$ = 1.4 and $CO_2/H_2S$ > 50. In addition, OVSG-IPGP also operates a network of three permanent MultiGAS stations at the summit (Cratère Tarissan, G56 and Cratère Sud). Nevertheless, this network, that was partly re-installed after September 2017 hurricanes, suffered further damages by hostile conditions. Therefore, the only reliable measurement in the period of interest is the concentration of $SO_2$ detected in the plume at Cratère Sud. Data available until 20 April 2018 show a net anomaly starting in early March 2018 and culminating at 1.9 ppm of $SO_2$ on 7 April 2018 (Fig. 12b). This early start of chemical perturbation is also observed in data from in-situ Giggenbach gas sampling on 23 March 2018, especially for $He/CH_4$ and to a lesser extent for $CO_2/CH_4$ (Fig. 11). It is important to note that the MultiGAS measurements show that the chemical perturbation is not only present at Cratère Sud but on the entire dome. These relatively high $SO_2$ levels at the Cratère Sud occur at the time when the aforementioned $SO_2$-rich signals were found in the periphery of the NAPN site (on 18–23 March 2018) and are correlated with portable MultiGAS data.

## 4. Data elaboration and discussion

### 4.1. Magmatic vs hydrothermal sources and the origin of overpressures: seismic and geodetic assessment

Fig. 5a shows the occurrence of clusters of seismicity increasing in frequency and rate until the 27–29 April swarm. Nevertheless, the seismicity until February 2018 is superficial, being in average observed down to a depth of 1 km b.s.l. (Fig. 5b), thus very distant from the supposed depth of the magma chamber (about 4.5 to 5.5 km b.s.l., or 6 to 7 km of depth below the summit; Pichavant et al., 2018, Villemant et al., 2014). This seismicity comes from the interactions between the flow of heat and gas from the magma at great depths and the presence of superficial phreatic groundwater layers in the volcano. Multiple factors (changes in fracturing, changes in pressure, flow, and temperature of gases, variation in the proportion of liquid water and gas, variation in
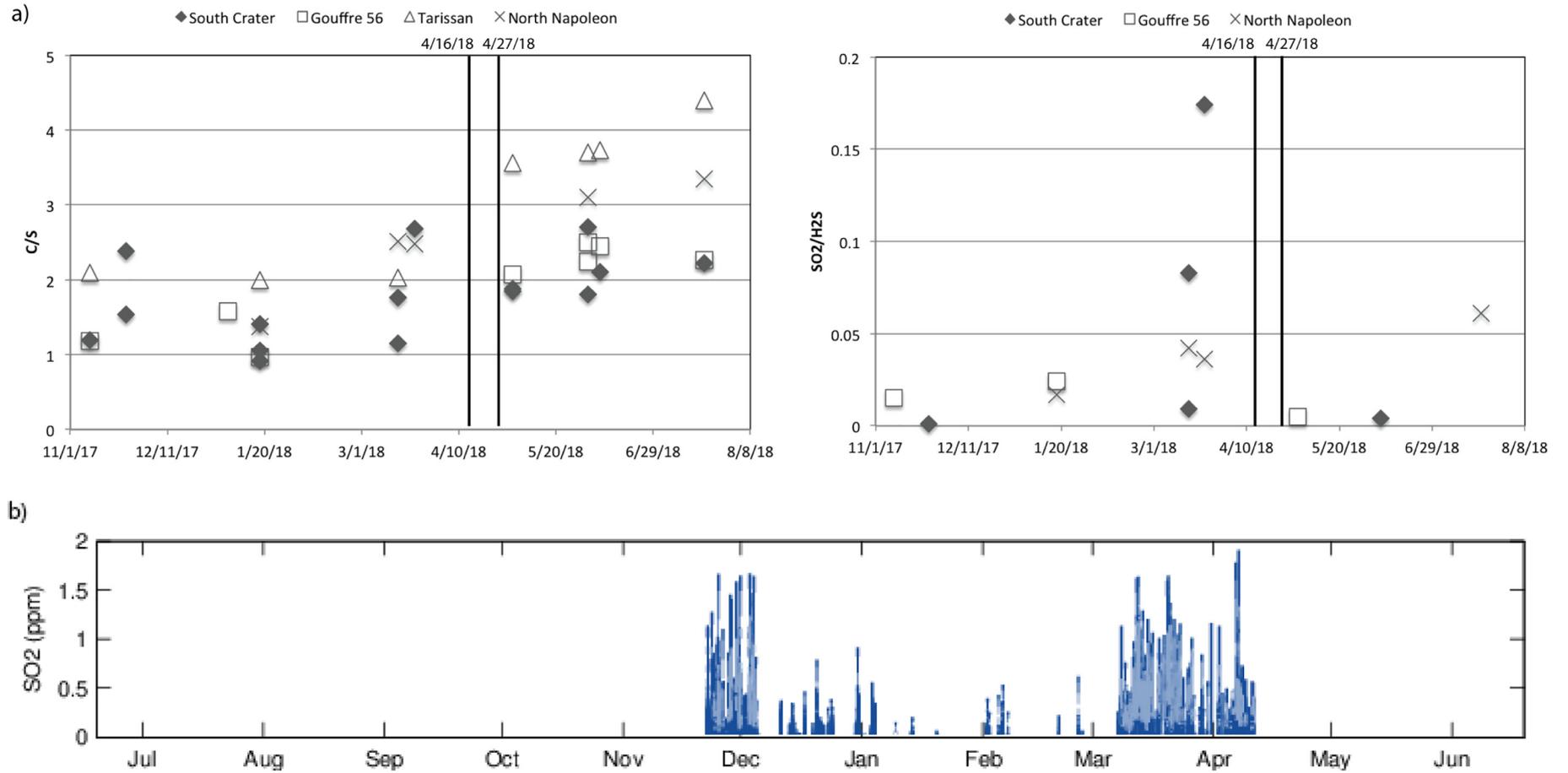
**Fig. 12.** SO₂ concentration and concentration ratios at major fumarolic vents (Figs. 1,2). Panel a) Chronogram of the C/S ratio (portable MultiGas station) at South crater (CSC and CSS vents), NAPN, G56, Tarissan crater lake (TAS). Panel b) Chronogram of SO₂ concentration (ppm) at South Crater (permanent MultiGas station).

the interaction depth between gases and liquid water) locally generate overpressures that favor an accumulation of deformation until the rock breaks. The corresponding waveforms are of hybrid-type, generally with a long period coda (Fig. 4). It is therefore the activity of the (shallow) hydrothermal system in the broad sense that seems to be at the origin of the typical La Soufrière seismicity, which translates into a weak total dissipated energy (Fig. 5) and does not testify to a deep reactivation of the volcano or to major modifications of its geomechanical response.

Values of the compressional to shear wave velocity, Vp/Vs, were estimated by the slope of P and S arrival time differences as a function of P arrival time (Wadati, 1933) and plotted versus the time to evaluate variations of the medium properties (Fig. 13). The red line in figure represents a moving average of 50 consecutive seismic events. Although an average Vp/Vs value of 1.74 (Fig. 13b) can be estimated, in agreement with the regional value of 1.73 reported by Bazin et al. (2010), Fig. 13 displays major Vp/Vs fluctuations differentiating the 2017 activity from that of January to July 2018. The 2017 activity is in fact characterized by Vp/Vs ratios up to 1.8, whereas two major negative Vp/Vs anomalies (Valley 1 and Valley 2 in Fig. 13) can be observed from December 2017 to the end of February 2018 and from the end of March 2018 to the beginning of June 2018. Highest values in 2017 occur when activity is lowest, i.e. prior to September 2017 (see also Fig. 5a). A significative decrease the Vp/Vs ratio is observed since the early January 2018 seismic activity peak (V1 in Fig. 13; see also Fig. 5a and Supplementary Fig. S1) giving rise to a negative anomaly in concomitance to the February 2018 seismic swarm (Valley 1, with lowest Vp/Vs at 1.64; Fig. 13), which occurred within the hydrothermal system below the dome. High Vp/Vs ratios are recovered in March 2018, but a strong decrease is then observed since the last week of March 2018, which gives rise to a second negative anomaly (Valley 2, with lowest average Vp/Vs at 1.61; Fig. 13) that lasts until the end of June 2018 and that includes the off-axis seismic swarms that started on 16 April and 27 April 2018. The beginning of this second anomaly is related to the intensification in seismicity observed before the 16 April 2018 swarm (V2 in Figs. 13, 5a) and occurs when fumarole steam fluxes where highest (Fig. 10) and temperature peaks were measured at Cratère Sud fumaroles (23 March, Fig. 9) and in the dry vent surrounding the NAPN fumarole, along with increased $SO_2$ contents (Fig. 12).

The observed Vp/Vs ratios are representative of the volcanic highly fractured, fluid-filled, rocky medium. Vp/Vs variations are then related to the mechanical reaction of the volcanic medium to pore fluid flow, hence to the joint effects of hydrothermal dynamics and hydrological forcing. The two negative Vp/Vs valleys reflect the fact that rock saturated with water at a temperature near water-steam transition would result in a large change in Vp, a small change in Vs, and a large change in Vp/Vs, as reported in Sanders et al. (1995) and shown by experiments conducted by Spencer Jr. and Nur (1976) and Ito et al. (1979). This is consistent with the evidence that high hydrothermal activity, is the main cause of the velocity anomalies (low Vp, low Vs, and low Vp/Vs)

beneath active volcanoes (Chatterjee et al., 1985; Walck, 1988; Nugraha et al., 2019), also favoured by the large aspect ratio (−0.1) of water-filled cracks (Nakajima et al., 2001).

Therefore, it seems that the observed seismicity reflects the weakening of the rocky medium due to fluid infiltration and hydrofracturing, determined by the increase of pore pressure (e.g., Nakamura, 1977; Miller et al., 1996; Miller and Nur, 2000; Sibson, 2000; Terakawa et al., 2010). Pore pressure increase on infiltration is not necessarily homogenous, and when it is localized into a narrow source, seepage forces originate that modify locally the stress-state (Mourgues and Cobbold, 2003; Rozhko et al., 2007). However, recovery of the Vp/Vs ratio, hence of nominal rock properties, was rapid after the 1 st February swarm, while it was much slower after the 27–28 April 2018 swarm and still incomplete in July 2018. This is related to the high energy of the 27 April $M_L$ 4.1 earthquake (Fig. 5c), with the involvement of a much larger seismogenic volume.

Geodetic data in the Basse Terre sector show that, down to a depth of 8 km b.s.l., the measured inflation is not associated with large intrusions. In addition, the nearly radial shape of the (shallow) dome deformation (Fig. 7a) suggests that deformation is associated to fluid overpressures within the hydrothermal system (e.g., Battaglia et al., 2006). The pattern of dome radial spreading is however perturbed by the detachment of the southwestern sector over 1.3 km of distance at a speed of 5–7 mm/year. This is consistent with imaging by electrical-resistivity tomography (Rosas-Carbajal et al., 2016), and with the superposition of three major fracture systems (Northern Fault, the Napoléon-56-Breislack system, and the Dolomieu system; Fig. 1) which divide the whole dome in three major blocks. In agreement with extensometric data (Fig. 8), rapid pressure fluctuations of the hydrothermal system may determine a differential response of each block, particularly the emergence of a mechanism of simple shear, more superficial and important during low-pressure phases when the perturbation to the radial, symmetric, deformation is largest and produces the closure of some fractures (Fig. 8).

One might expect that observed deformations and seismicity are related to the switch from drained to undrained conditions of the boiling hydrothermal system and of shallow phreatic fluids circulating through the porous medium. Under undrained conditions, rapid pore pressure build-up takes place until the occurrence of hydraulic fracturing breaks the host rock; as testified by the low Vp/Vs values observed in April 2018 (Fig. 13). Nakamura (1977) first suggested that hydraulic fracturing is an important process in generating volcano-hydrothermal seismicity and in the case of La Soufrière de Guadeloupe this argument was invoked by West et al. (1978). Hydraulic fracturing of a rock occurs when the effective fluid pressure overcomes the tensile strength of the rock and any confining pressures. This is expressed as $P_b = 3\sigma_3 - \sigma_1 + T - P_0$ where $P_b$ is the formation breakdown pressure of rock of tensile strength T at a pore pressure $P_0$ in a compressive stress field with $\sigma_3$ and $\sigma_1$ the minimum and maximum principal stresses, respectively, on the plane orthogonal to the infiltrating fluid stream
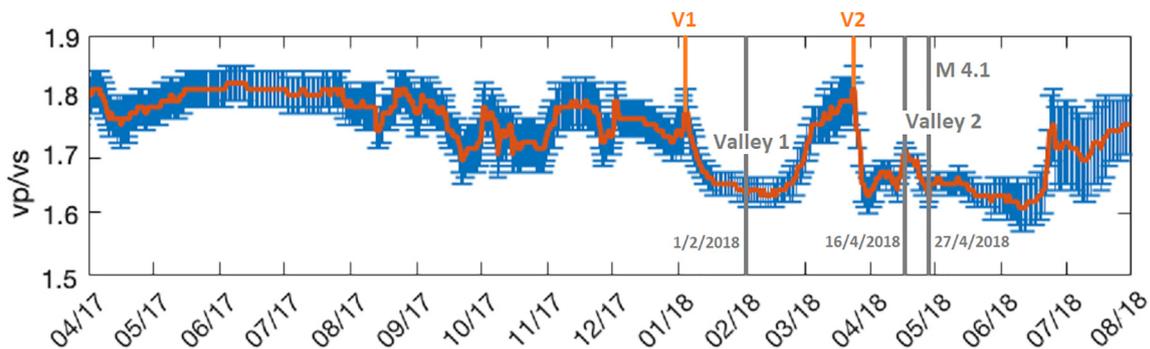


**Fig. 13.** Chronogram of Vp/Vs ratio, calculated from the Wadati method (1933) (panel c). Solid lines in each panel represent moving averages of 50 events, according to the expression for seismic rate (see text).

(Kehle, 1964). Only fluids with a low viscosity, such as steam, have a great ability to influence the pore pressure $P_0$ and reducing the pressures necessary for fracturing. In addition, low viscosity fluids can open existing fractures even if their orientation is other than parallel to the maximum principal stress (Zoback et al., 1977). This is the reason why some fractures and faults of the summit (including the 8 Juillet and Napoléon faults) behave very dynamically, as observed via extensometric measurements.

It must be noted that the rate of pressurization also affects the breakdown pressure, a high rate of pressurization resulting in an anomalously high breakdown pressure (Haimson and Zhao, 1991; Schmitt and Zoback, 1992). As the rate of pressurization increases, in a volcano, the mode of deformation may change from viscous to plastic and then to elastic, at high rates of pressurization (West et al., 1978). We then definitely hypothesize that the rapid pressurization determined by the onset of undrained conditions led to the $M_L$ 4.1 (or $M_w$ 3.7) earthquake of 27 April. Indeed, its focal mechanism and features (see Supplementary Material and Supplementary Fig. 6) identify a NW-SE normal fault dipping ~40° to the NE (Fig. 14), coherent with active regional faults (Feuillet et al., 2011). Shallowly dipping faults in extensional tectonic regimes are known to be reactivated by elevated fluid pressure (e.g., Collettini and Barchi, 2002; Sibson, 1990, 2000; Micklethwaite and Cox, 2006; Cox, 1995; Terakawa et al., 2010) and variations of fluid pore pressure related to hydrothermal fluid circulation are known to explain seismic activity in volcanic environments (e.g., Ventura and Vilardo, 1999 and references therein). A good analogy is offered by the seismic activity of Mount Vesuvius (Italy), particularly its 9 October 1999 earthquake ($M_L$ = 3.6), for which no significant departure of the fault mechanism from a double-couple source can be inferred (Del Pezzo et al., 2004; Zollo et al., 2002).

The epicentres of 16–17 and 27–29 April 2018 swarms, although separated by an aseismic segment (Fig. 6b, Supplementary Figs. 3,4), define a structure whose direction is that of all the active regional faults that cut the volcanic arc and cross the Basse-Terre through the La Grande Decouverte-Soufrière complex (Fig. 1). A fault of the same orientation has so far not been mapped in this area, perhaps because hidden by recent volcanic deposits. We suggest that the hybrid waveforms of the 16–17 swarm and especially of the subsequent ~30

hybrid events, point to invading high-pressure fluids along the shallowly dipping NW-SE structure, which may have locally weakened the fault through the rapid reduction (on the scale of days) of the effective normal stress acting on the fault plane (e.g., Collettini and Barchi, 2002; Sibson, 1990; Terakawa et al., 2010; Rozhko et al., 2007). We also suggest that the lack of spatially continuous seismicity between 16 and 17 and 27–29 April swarms can be explained by a change in dilatation and pore pressure polarity (contraction at the 27–29 April site, expansion in the 16–17 April one, near the La Soufrière de Guadeloupe dome), in line with the explanation provided by Miller et al. (2010) for the lack of seismicity observed in 1995 at Montserrat along the structure connecting the Soufrière Hills volcano and the St. George Hills.

Feuillet et al. (2011) have studied the collocation of active and recent volcanic vents (e.g., La Soufrière of Guadeloupe and Soufrière Hills, Montserrat) and faults in the Lesser Antilles arc, and have shown that faulting and volcanism are organically connected and likely interact, through coupling mechanisms determined by static or dynamic stress changes (e.g., Brodsky et al., 1998; Nostro et al., 1998; Linde and Sacks, 1998; Hill et al., 2002; Marzocchi, 2002; Troise, 2001; Walter and Amelung, 2007 and references therein). It appears in fact that such coupling mechanisms can lead to unrest or eruptions within few days, months, and perhaps years at neighbouring volcanoes (Nostro et al., 1998; Watt et al., 2009).

### 4.2. Magmatic vs hydrothermal sources and the origin of fluid pressures: geochemical assessment

#### 4.2.1. Gas end-members and secondary processes

The elements shown and listed so far clearly point out an indirect forcing of deep hydrothermal and/or magmatic origin. A first increase in $SO_2$ content and in $SO_2/H_2S$ via MultiGAS (Fig. 12), and in fumarolic $CO_2/CH_4$ and $He/CH_4$ (Fig. 11c,d), was in fact seen on 23 March. The further sharp evolution leading to the peaks in the $He/CH_4$, $H_2/H_2O$ and $CO/CO_2$ ratios (Fig. 11d–f) that occurred in concomitance with the 27 April 2018 highly energetic earthquake ($M_L$ 4.1), suggests that a direct link exists between the heating and overpressurization of the hydrothermal system and the rock failure process. This is very likely in relation with the thermal and pressure perturbation of hydraulic boundaries at
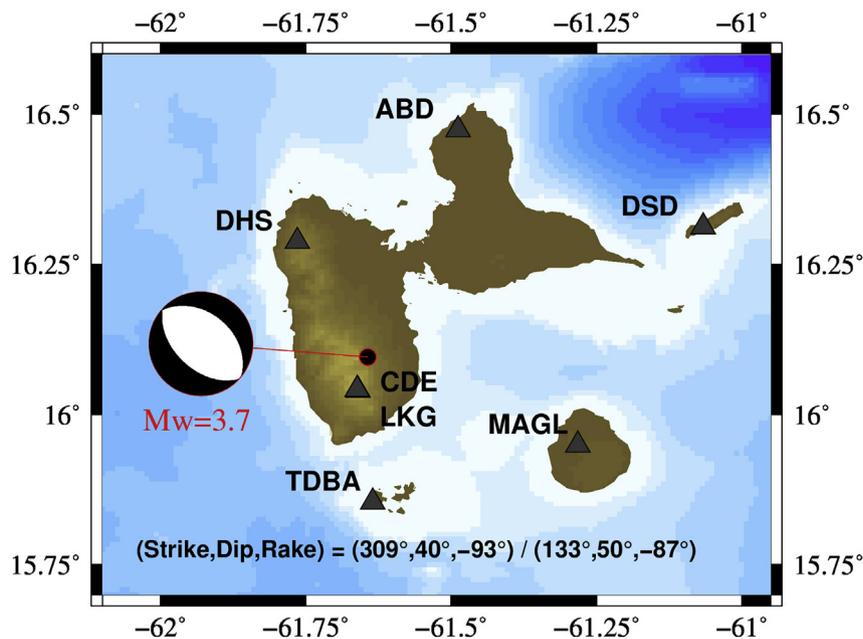


**Fig. 14.** Focal mechanism and moment magnitude of the 27 April $M_L$ 4.1 earthquake. The 3-component displacement waveforms provided by the 7 seismic stations (indicated by triangles) were used for source parameter determination. The MECAVEL waveform-based method (see Supplementary Material) retrieves an $M_w$ = 3.7 moment magnitude and a pure normal-faulting mechanism, whose strike, dip and rake (for the two possible planes) are shown on the map. The optimal epicentral location (lat = 16.08, lon = −61.66) is consistent with the location determined by arrival times (lat = 16.06, lon = −61.67), given the frequency range used in the inversion (0.04–0.7 Hz).
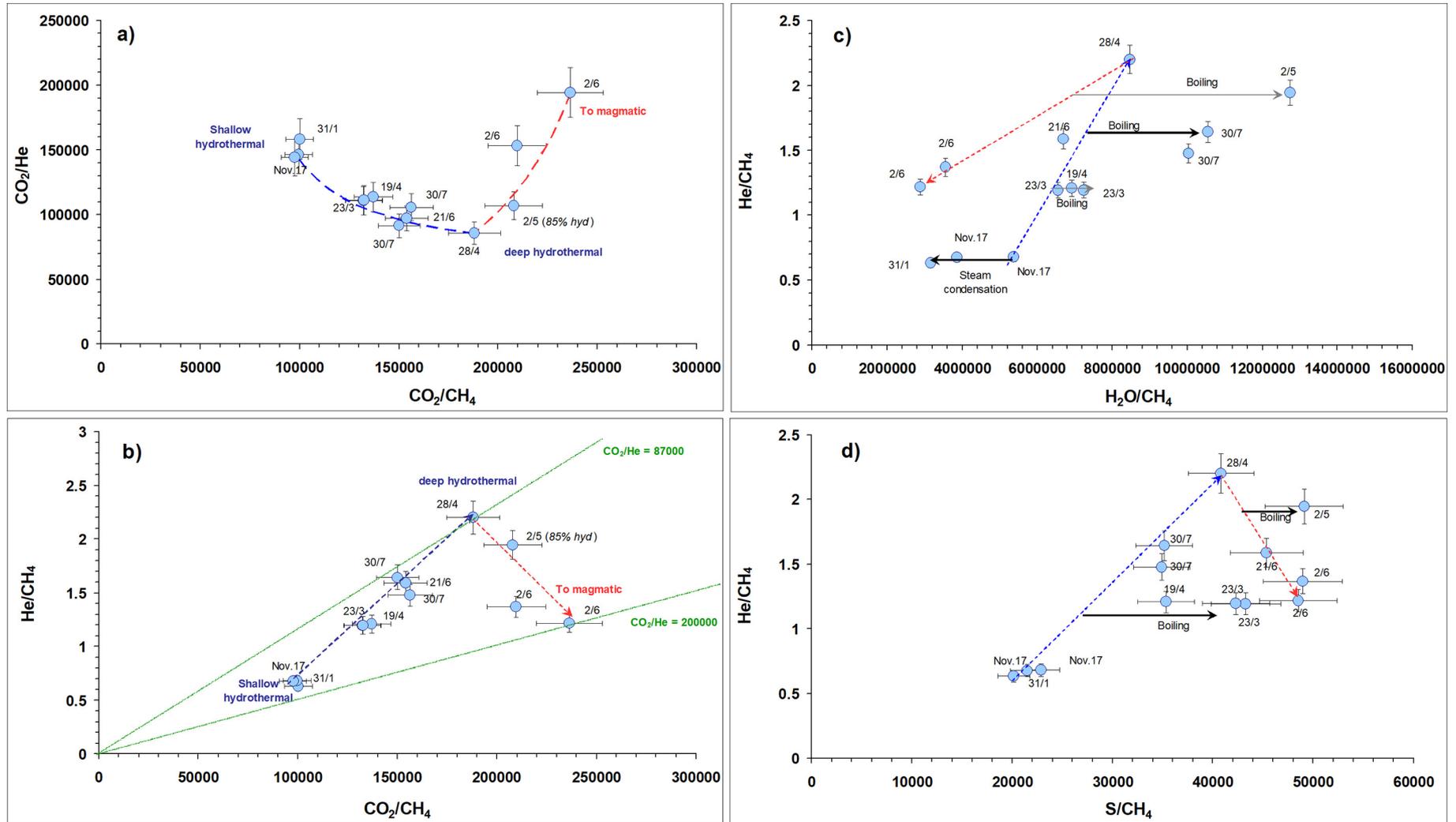
**Fig. 15.** Covariation of $CO_2/He$ with $CO_2/CH_4$ (panel a), $He/CH_4$ vs $CO_2/CH_4$ (panel b), $He/CH_4$ vs $He/H_2O$ (panel c) and $He/CH_4$ vs $He/H_2S$ (panel d), showing a He-rich hydrothermal component (meteoric-local hydrothermal line) mixing with a deep, magma-derived gas component. Secondary effects due to either steam condensation or boiling can be observed in panel c. These effects due to either scrubbing or hydrothermal sulphur remobilization can be observed in panel d. See Supplementary Material for discussion on error bars, which are within symbol size if not shown.

depth due to the arrival of deep gas pulse(s). This produced an enhancement of boiling, which however contrasts with the very low fluxes observed at CS fumaroles, CSC particularly, since late April, and the concomitant temperature drop to values consistent with water boiling at the local atmospheric pressure (~95 °C). This(these) gas pulse (s) was(were) released until 2 June 2018 at least, when maxima in the gas/steam and $CO_2/CH_4$ ratios were observed (Fig. 11a,c).

In order to discriminate between the different gas end-members (e.g., meteoric, hydrothermal, magmatic) and understand more how they do interact, we first look at the covariation of compositional indicators (e.g. $CO_2/He$, $He/CH_4$, $CO_2/CH_4$) which are not appreciably affected by secondary hydrothermal phenomena (steam condensation, boiling, component scrubbing, remobilization, precipitation). The relative effect of these secondary phenomena can then be assessed by enlarging the approach to indicators such as $S/CH_4$ and $H_2O/CH_4$. On this basis, Fig. 15a,b shows that fumarolic fluids prior to the $M_L$ 4.1 event of 27 April 2018, follow a mixing line (dashed lines in all panels), characterized by a $CO_2/He$ ratio evolving from 150,000 (November 2017 and 31st January 2018 samples) to 87,000 (28 April 2018 sample). Along this mixing line, increasing $CO_2/CH_4$ reflects an approach towards the hot and oxidized conditions typical of the deeper hydrothermal component, which then boils off in the roots of the volcanic dome upon interaction with the oxidized, nearly $CH_4$-free, magmatic gases. This is accompanied by the $CO_2/He$ decrease (panel a) and $He/CH_4$ increase (panel b), which point to a He-rich deep hydrothermal component. The helium enrichment of the local deep hydrothermal system can be ascribed to the long-term interaction of the deep hydrothermal fluid with magmatic rocks and the accumulation of radiogenic He, as well as to the contribution of a basal flux mostly determined by a contribution of background andesitic magma degassing. On the other hand, the shallow hydrothermal component is enriched in the very He-poor meteoric component.

We do not know hitherto the chemical composition of the hydrothermal liquid phase that contributes to the groundwaters circulating in the volcanic complex (Ruzié et al., 2012, 2013; Villemant et al., 2005, 2014) and, that underneath La Soufrière dome, boils off the fumarolic fluids discharged at the volcano summit. However, it is highly probable that the deep hydrothermal fluid is a NaCl aqueous solution (Brombach et al., 2000; Villemant et al., 2014). These fluids readily form in active volcanic environments through (1) the absorption of $SO_2$ and HCl-rich magmatic gases in deeply circulating groundwaters and (2) neutralization of these initially acidic groundwaters by reaction with wall rock containing minerals capable of neutralizing acids, such as feldspars, micas, and other silicates (Giggenbach, 1988, 1997; Reed, 1997. Chiodini et al., 2001). The (deep) NaCl-rich hydrothermal aquifer in its portion surrounding the dome is boiled off upon receiving a considerable input of fluids from a degassing magma body (4.5 to 5.5 km b.s.l., or 6–7 km deep below the dome summit; Pichavant et al., 2018). It then mixes with fast circulating meteoric waters having an average residence time of three months (Bigot et al., 1994). This results in the shallow-to-deep local hydrothermal trend of Fig. 15.

Fig. 15a,b show the presence of another mixing line (red dashed lines in all panels), which we identify as that trending to the more magmatic end-member characterized by the high $CO_2/CH_4$ ratios (2 June samples, see also Fig. 11c), but also $CO_2/He$ and $He/CH_4$ ratios higher and lower, respectively, than those of the gas discharged on 28 April (assumed representative of the deep hydrothermal component). This new gas of magmatic origin is different from the one typically interacting with the hydrothermal system because it is characterized by a much larger $CO_2/He$ ratio, consistent with degassing from a deeper or more compressed magma as $CO_2$ solubility is lower than He solubility in basaltic and andesitic magmas (Nuccio and Paonita, 2000; Caliro et al., 2014). The release of this new gas component becomes evident in the 2 May sample and reaches its maximum in the 2 June samples, which were particularly steam-poor and $CO_2$-rich (Table 1; Fig. 11a,c). Using the steam-poorest composition from 2 June sampling as the new gas

end-member and the 28 April one for the hydrothermal end-member, we estimate 85% of the 02 May sample consists of the hydrothermal component (Fig. 15a,b).

Hence, the behaviour of $CO_2/CH_4$, $CO_2/He$ and $He/CH_4$ ratios suggests that a magmatic gas deeper than that usually soliciting the hydrothermal system has intervened and led to the unrest episode recorded between February and late April 2018. Therefore, this gas, discharged after the seismic peak of 28 April, heated up and then pressurized the hydrothermal system prior to becoming detectable at the fumaroles. This mechanism explains the $He/CH_4$, $H_2/H_2O$ and $CO/CO_2$ peaks (Fig. 11d–f) roughly concomitant with the $M_L$ 4.1 earthquake and should imply increasing boiling of the hydrothermal system feeding summit fumaroles. Fig. 15a,b also highlights that after having discharged the "anomalous" deep magmatic gas, fluid compositions returned along the hydrothermal mixing line (21 June and 30 July samples). However, pre-crisis conditions (e.g. November 2017) are not fully regained and sample position along the trend (close to the 28 April values) suggests an important residual deep hydrothermal component.

The $He/CH_4$ vs $H_2O/CH_4$ covariation in Fig. 15c shows both negative and positive departures from mixing trends identified in Fig. 15a,b. Negative departures represent steam condensation, and affect early samples (November 2017, 31 January 2018) as well as the 21 June one, which marks the return of the fluid system along the hydrothermal trend. On the other hand, positive departures of the $H_2O/CH_4$ ratio mean increased boiling with respect to the hydrothermal trend. These are observed for 23 March 2018 (when fumarole temperature reached 111 °C, Fig. 9a), 19 April 2018, but also for 30 July samples. However, the most important boiling effects are seen for the 2 May composition, especially considering that these results by mixing with the "anomalous" magmatic gas that started to be discharged after the seismic peak. It must be noted that the evolution of any hydrothermal system from depth to surface is most likely characterized by a multi-step sequence of secondary processes such as boiling and steam condensation. These are nearly invariantly present at La Soufrière's summital fumaroles, in light of the vent temperature normally buffered by coexisting liquid and vapour at the local atmospheric pressure (Fig. 9a,b). Nevertheless, the information provided by Fig. 15c summarizes the dominant secondary effect with respect to the current standard conditions occurring along the trends identified in Fig. 15a,b.

Similarly, Fig. 15d allows us to evaluate that secondary effects influencing sulphur concentration (scrubbing versus remobilization of the stored hydrothermal sulphur. It shows that hydrothermal sulphur was remobilized on 19 April, and particularly on 23 March, when anomalous temperatures and degassing were measured in the surrounding of the NAPN site (Fig. 1), with the dry emission of $H_2S$ and $SO_2$ in nearly equal amounts measured by Multigas (Fig. 12). This likely resulted from the start of the heating cycle due to the arrival of relatively high-temperature fluids, which led to the local remobilization of the earlier deposited elemental sulphur ($S_e$) according to the following reaction (Mizutani and Sugiura, 1982; Giggenbach, 1987):

$$3S_e + 2H_2O \Longleftrightarrow SO_2 + 2H_2S \qquad (3)$$

In addition, the difference in C/S ratios measured by MultiGAS between CS and G56 on one side, and Tarissan and NAPN on the other one (Fig. 12a), is likely the result of the larger sulphur scrubbing operated by the acid lake (Tarissan) and the shallow circulating groundwaters (NAPN) with respect to CS and G56 sites.

In Fig. 15d, the 2 May fluid composition appears to be enriched in sulphur with respect to the mixing trend of deep local hydrothermal and magmatic components, in agreement with the boiling effect described in Fig. 15c. Instead, the position of datapoints from 21 June and 30 July, close to each other and along the mixing trend of deep local hydrothermal and magmatic components, contrasts with the findings of Fig. 15c (steam condensation and boiling dominant on 21 June and 30 July, respectively). It also appears that their $S/CH_4$ ratios are

akin to the one due to the mixing of the deep local hydrothermal gas and the "anomalous" one of deep magmatic origin. Following Giggenbach (1980), it is in fact possible that the many secondary reactions involving sulphur modify the simple picture associating boiling to sulphur remobilization and steam condensation to sulphur scrubbing.

Following the approach described in Moretti et al. (2013a, 2017), the occurrence of perturbations on the hydrothermal equilibrium involving total sulphur as $H_2S$ can be identified by considering the following equilibrium:

$$2H_2S_{(g)} + FeO_{p.r.} \Longleftrightarrow FeS_2 + H_2O_{(a)} + H_{2(g)} \qquad (4)$$
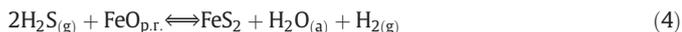
in which $FeO_{p.r.}$ refers to a generic oxide component of divalent iron in the pyroclastic rocks, $FeS_2$ is the pyrite component of sulfide solid phases of the hydrothermal system and the superscripts (a) and (g) refer to aqueous solution and gas, respectively. By considering that activities of $FeO_{p.r.}$ and $FeS_2$ can be considered constant because fixed by average rock compositions of the hydrothermal systems and that $H_2O$ activity is constant and also close to unity for the system of interest, the equilibrium constant reduces to:

$$logK_4 = log\frac{[H_2]}{[H_2S]^2} + const. \qquad (5)$$

A hydrothermal system not perturbed by anomalous heating and oxidation phenomena, for example related to the arrival of magmatic gases, should display constant $logK_4$ with time. Fig. 16 then suggests that the usual hydrothermal equilibrium conditions recorded at the CSC fumarole ($logK_4 \approx 0$ in Fig. 16) appear being definitely perturbed in concomitance with the 16–17 April 2018 swarm. An increase of $logK_4$ is in fact observed until 2 May, implying that the hydrothermal system experiences a relative increase of $H_2$ due to the temperature raise and boiling. The perturbation becomes negative on 2 June, reflecting the arrival of the deep "anomalous" gas (corresponding to the gas/steam and $CO_2/CH_4$ peaks, Fig. 11a,c), which injects additional sulphur and oxidizes the system. On late June 2018 the perturbation on $logK_4$ has disappeared.

### 4.2.2. Thermal and baric evolution of the hydrothermal system

To understand more about the thermal (T) and baric (P) anomalies associated with the progressive arrival of the deep gas, the thermochemistry of discharged fluids must be considered, in order to calculate the P-T conditions of the boiling hydrothermal reservoir. From the chemistry of fumarolic gases, we then compute the P-T conditions of the boiling hydrothermal system feeding summit fumaroles following Chiodini and Marini (1998) (Fig. 17). This method is based on the sum of log ratios between pairs of species making up redox exchanges in

the gas phase and accounts for the fact that multiple oxidation states may be active within the hydrothermal system and that all species ($H_2O$-$CO_2$-$CH_4$-$CO$-$H_2$) attain the condition of chemical equilibrium (Chiodini and Marini, 1998; Moretti et al., 2017).

From the 1997 data (Brombach et al., 2000) appearing in the diagram of Fig. 17, but for which methane was undetected, we estimated a detection limit concentration of 0.1 μmol/mol, based on the data from the Authors. The vertical error bars cover two orders of magnitude in $CH_4$ concentration (0.01 to 1 μmol/mol) and show the low-weight that this species has on $3log(CO/CO_2) + log(CO/CH_4)$ (Chiodini and Marini, 1998). Similarly, 1976 data (Chevrier et al., 1976) were plotted by considering, conservatively, a $CH_4$ detection limit of 1 μmol/mol and a vertical error bar covering two orders of magnitude (0,1 to 10 μmol/mol). Note that vertical error bars for CSC samples include data dispersion on concentration measurements from replicate samples. Therefore, they are highly conservative and greatly exaggerate the purely instrumental error, which is contained within symbol size.

Fig. 17 shows that CS samples plot within the two-phase field, and that fluids sampled on 28 April 2018 (few hours after the earthquake) and 2 May 2018 fall very close to the critical point of pure water (CP; 374 °C, 220 bar). Within the two-phase field, boiling occurs and the gas separates from the liquid, theoretically by an isenthalpic process of single-step vapour separation (svss, Chiodini and Marini, 1998). Under this approximation, each sample represent a vapour which falls on a svss line related to the original temperature and pressure of the corresponding boiling liquid on the saturated liquid line (Fig. 17).

This does not mean that the rising hydrothermal fluid does not experience multiple sequential secondary processes, such as vapour gain or loss and multi-step vapour condensation and separation. However, when falling within the two-phase field, measured data are in agreement with an isenthalpic single step vapour separation, which includes all intervening secondary effects and implies that boiling is the dominant one. We notice that the fluid system points to an original boiling liquid normally at 340 °C and that since November 2017 the conditions of gas separation have shifted towards the saturated vapour line, i.e. very close to the P-T condition of the original boiling liquid. Assuming the simple scenario of single-step isenthalpic vapour separation, we find that the P-T peak is recorded by the 2 May sample, which represents a vapour separated at 350 °C from a liquid phase originally at 370 °C and 210 bar. The fraction of separated steam from the boiling liquid is 21 mol%. Afterwards, the hydrothermal system relaxes, experiencing a P-T decrease, until 30 July samples, when pre-crisis P-T conditions seem to be restored. Fig. 17 thus confirms the hypothesis that the boiling hydrothermal system was thermally solicited up to the critical point of water. Because of the low sampling frequency, we do not know if the critical point of water was finally exceeded, as was seen for July 1976 samples (Chevrier et al., 1976), but this is likely to have occurred. However, the supercritical excursion recorded by 1976
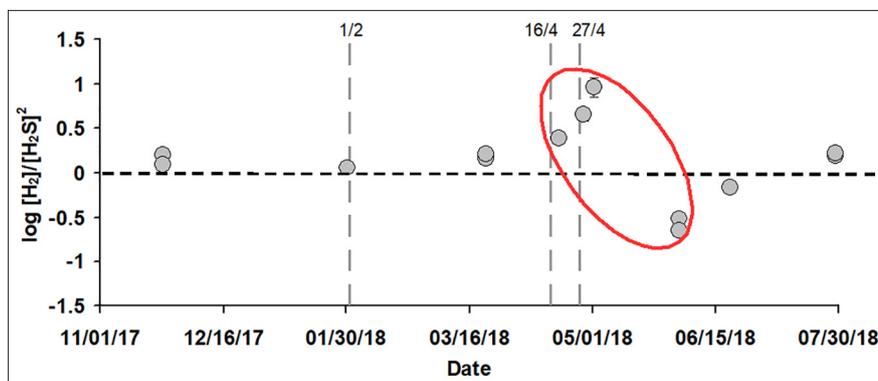


**Fig. 16.** Chronogram of the hydrothermal sulphur equilibrium (Moretti et al., 2013a, 2017), showing the April perturbation (red ellipse). $H_2S$ is used for total sulphur. (For interpretation of the references to colour in this figure legend, the reader is referred to the web version of this article.)
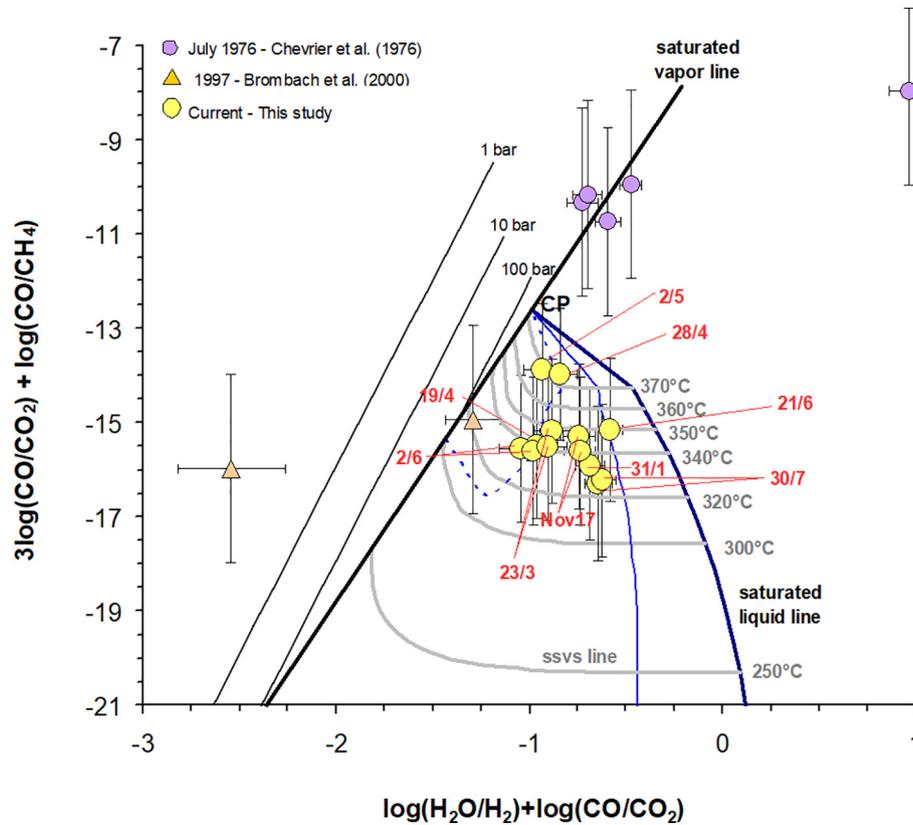
**Fig. 17.** Plot of the sum of chemical log-ratios within the $H_2O$-$CO_2$-$H_2$-$CO$-$CH_4$ system. See Chiodini and Marini (1998) for details on the construction of the diagram. Present-day data plot within the field of boiling liquids and represent separated vapour phases. Note that data tend to define a baseline at 340 °C, corresponding to the base temperature of the current hydrothermal liquid. Different single-step vapour separation (svss) lines are plotted for different temperatures, connecting the saturated liquid and the saturated vapour. Blue lines are common loci for vapour separation occurring at 100 °C (solid line) and 300 °C (dashed line). Horizontal error bars are ±11%, or within symbol size if not shown. For CSC sample, vertical error bars are ±10%, or within symbol size if not shown. In both cases, errors account for the average long-term external reproducibility on gas concentration measurements in our laboratory, by averaging measurements on replicate successive samplings. Therefore, they greatly exaggerate the purely instrumental error, which is contained within symbol size. See also Table 1 for errors on concentration measurements and the Supplementary Material for additional details. For data from Brombach et al. (2000) and Chevrier et al. (1976) error bars are given by the strong uncertainty in $CH_4$ content (see text). (For interpretation of the references to colour in this figure legend, the reader is referred to the web version of this article.)

data might also reflect separation from a NaCl-brine, whose critical point would be located along the saturated vapour line at temperatures higher than that of pure water (Chiodini et al., 2001). Under both hypotheses (supercritical excursion of pure water vs boiling of a brine), it is supposed that the hydrothermal reservoir feeding the 1976 eruption was much more sealed than the present one (Boichu et al., 2011; Komorowski et al., 2005; Villemant et al., 2014), such that it could either rise in temperature and pressure more easily than currently, or let much less meteoric component to be introduced and to dilute the locally boiling liquid (water or brine). In all cases, the hydrothermal system has clearly evolved since 1997, when steam condensation upon cooling (i.e.; high $H_2/H_2O$ ratios in 1997, Fig. 11e) was the dominant secondary process, as demonstrated by datapoints falling on the left of the saturated vapour line (Fig. 17). Steam condensation thus favoured the growth of the very shallow hydrothermal system, accompanying the formation of acid ponds (Komorowski et al., 2005). Nevertheless, the continuous forcing of magmatic gases, has in time favoured boiling, progressively embracing circulating shallow groundwaters of meteoric origin.

Figs. 11, 15, 16 and 17 show that at the end of June 2018, the hydrothermal system seems to return to the pre-crisis situation observed in late 2017. Given the infiltration of magmatic gases into the hydrothermal system, as well as the high temperatures and pressures inside the hydrothermal system, we believe that the volcanic system was at that time being recharging and was accumulating energy. Additionally, Fig. 17 suggests that the present-day hydrothermal system is in a pre-

1976 condition, such that additional overpressure peaks associated with deep pulses of magmatic gas may destabilize the hydrothermal system and lead to phreatic explosive activity, such as in 1976.

At present, we cannot establish exactly the origin of the deep "anomalous" gas and the mechanism determining its release and ascent into the hydrothermal system. Nevertheless, two reasonable hypotheses can be formulated given our analysis of conjugated chemical indicators based on conservative gas species in the discharged fumarolic fluids:

1) the deep "anomalous" magmatic fluid is stored at mid-to low-crustal depths and when a relevant amount is reached, it is transported upward via buoyancy-driven or pressure-driven flow mechanisms (Norton and Knight, 1977; Connolly, 1997). This takes place through a surrounding ductile medium, the brittle-ductile transition being likely located at around 1.5 km b.s.l. (3 km below the Soufrière summit) based on the geochemical conceptual model of Villemant et al. (2014). This deep upstreaming gas fluxes the shallow cooling and crystallizing magma body remnant of the 1530 eruption through cyclic mechanisms rejuvenating its exsolution behaviour (Boichu et al., 2008, 2011; Moretti et al., 2013a, 2013b, Moretti et al., 2019).

2) The deep "anomalous" magmatic fluid is released in pulses each related to episodes of fresh injections of basaltic magma in the long-lived (up to thousand years) andesitic chamber located at 4.5 km b.s.l. (6 km depth below the summit, Semet et al., 1982; Touboul et al., 2007. Poussineau, 2005; Pichavant et al., 2018). However, such inputs are likely, too small to be detected by the current

geophysical instruments. Notably, $^3$He/$^4$He determinations in fumarolic and hot spring gases and considerations on the thermal evolution of springs, together with the observation of contrasting halogen behaviour in spring waters and fumarolic condensates, point to recurrent injection of fresh basaltic magma (Ruzié et al., 2012; Villemant et al., 2014). Archetype examples of these fresh magma injections would be the one triggering the 1976–77 phreatic crisis, and another one, of smaller size that marked the onset of the long-lasting current unrest around year 1992 (Villemant et al., 2014).

It is of course possible that observed deep magmatic pulses are related to a combination of these two scenarios. Nevertheless, as far as the unrest sequence observed in 2018 were to reoccur, this might escalate to a magmatic phase following the initial phreatic activity, due to the availability of either *a*) rejuvenated magma in the shallow, 1.5 km b.s.l. deep, magma chamber (Villemant et al., 2014), or *b*) deep-sourced (≥4.5 km b.s.l.) fresh magma which in the future could directly supply the shallow reservoir.

### 4.3. Why the 2018 unrest episode must be regarded as a failed phreatic eruption

The evidence that hot springs do not record significant thermal and chemical variations, contrary to summit fumaroles, implies that the hydrothermal system is disconnected from shallower aquifers in the area surrounding the dome. In fact, summit vents are located along a dome axial zone of high vertical permeability due to faults and deep fractures. This allows the rapid ascent of the steam separated by one or more boiling aquifers whereas hot springs discharge from an outer zone, where groundwaters are heated through conduction or addition of small amounts of hot saline liquids coming from deeper hydrothermal aquifer(s) (Brombach et al., 2000; Ruzié et al., 2012, 2013; Villemant et al., 2014; Rosas-Carbajal et al., 2016), which are too small and readily absorbed.

For simplicity, we assume that the deep hydrothermal system below and surrounding the La Soufrière dome represents a continuum. Consequently, we relate the observed phenomena to the flow of water and steam, thus to the resulting competition between drained and undrained hydraulic conditions, which at the different sites is determined by existing hydrological boundaries (mainly permeability). Therefore, we propose that the P-T variations of the hydrothermal continuum yielded rapid pore pressure increase and undrained conditions particularly along the NW-SE fault structure activated during the 16–17 April and 27–29 April swarms, outside the La Soufrière dome. On the other hand, the fractures connecting the actively degassing dome summit area (a free-surface boundary condition) with the deep overpressured source at the base of the dome, allow the ascending fluids to be discharged and to remain at nearly hydrostatic pressure (Miller et al., 1996; Miller and Nur, 2000; Terakawa et al., 2010), thus approximating a drained condition. On this basis, Fig. 18 provides a conceptual model for the La Soufrière system and summarizes the main current features of the La Soufrière magmatic and hydrothermal system, as well as the temporal evolution through the recent unrest episode (see Supplementary Fig. 7 for a comprehensive picture of various changes and their timing).

In the representation of Fig. 18, we locate the pressure source below the dome by considering the P-T conditions of the hydrothermal liquid and right above the sealing cap marking the top of the brittle-ductile transition zone inferred at about 1.5 km bsl (Villemant et al., 2014). This sealing cap separates the lower plastic region where magma-derived fluids accumulate from the upper hydrothermal region, where fluids at hydrostatic pressure circulate through the brittle rock and maintain permeability via persistent seismicity (Fournier, 2007). The depth at which we place the sealing cap agrees with observations indicating that the brittle–plastic transition commonly occurs at about 370–400 °C within presently active continental hydrothermal systems

(Fournier, 2007). Considering that the high-magnitude VT seismicity is associated with breaching of the self-sealed zone (Fournier, 2007), we constrain the geometry of the brittle-ductile transition zone outside the volcanic axis by considering hypocentral depths of 16 and 27 April events just on top of it. A crystal mush extending downward from depths of 5 km bsl is pictured as the source of heat and deep fluids.

Boiling of the hydrothermal liquid separates the vapour responsible of the upward fluid circulation feeding the fumaroles and nurturing the shallow seismicity and deformation. Because the temperature of such a liquid is normally 340 °C (see Fig. 17), fluid pressure is 146 bar and liquid density 611 kg/m$^3$ (NIST, 2018). Hydrostatic conditions are then established with the free-surface at the top of the dome. Considering at first approximation a constant fluid density in response to the convective homogenization, we can calculate ($z = P/[g\rho]$) a source depth of 0.9 km b.s.L (or 2.4 km below the summit). This corresponds very well to the hypocentral depth of three most energetic earthquakes of 1 st February (1 km b.s.l.; OVSG-IPGP, 2018a). Based on 28 April and 2 May gas samples, which separate from a liquid originally at 370 °C (Fig. 17), we infer that this source was overpressured until reaching the critical point of pure water on 27 April 2018. Because the critical point occurs at P = 220 bar (NIST, 2018), an overpressure of 64 bar was attained in the source below the dome. Nevertheless, this overpressure in the dome roots was released aseismically. It is now worth recalling that the seismicity along fracture/fault planes infiltrated by fluids is produced by the instantaneous switch to large permeability values at the onset of cracking (Miller et al., 1996; Miller and Nur, 2000; Miller, 2015). Below the dome this process occurred evidently on February 1 st, but on 27 April the volcanic dome was able to restore aseismically the hydrostatic gradient because the overpressured source was already tapped by a network of structures with high vertical permeability and already critically stressed (i.e. the fractures and faults activated or created during the 1976 phreatic eruption, which modified the dome and reactivated since the 1992 onset of volcanic unrest; Komorowski et al., 2005; Ruzié et al., 2012; Villemant et al., 2014). These structures then lowered the tensional state of the volcanic edifice by discharging the accumulated overpressure. The latter is testified by the episodic locking of fractures measured in April 2018 (Fig. 8b), as well as by the behaviour of fumarolic temperatures and heat fluxes. These were in fact rapidly increasing since the beginning of the year and then started decreasing right after the 16–17 April swarm (Fig. 9), showing that the heat flux is not stored in different aquifers but is evacuated through the main fractures.

The "usual" La Soufrière hybrid micro-seismicity concentrated within the dome, between −1 and 0.5 km of depth b.s.l. (Figs. 5b, 6b; see also Ucciani, 2015, Ucciani et al., 2015). This depth range is likely determined by the mechanic interplay of volcano loading with the non-homogenous distribution of the permeability within the shallow network of fractures. This network, upon fluid circulation, continuously evolved being characterized by patches of opening cracks, and patches of sealing cracks, with the sudden recovery of permeability (Miller et al., 1996; Miller and Nur, 2000; Fournier, 2007; Miller, 2015). Nevertheless, one major question is why this shallow microseismicity was not observed for a long time following the late April 2018 swarm. Diffuse hybrid seismicity (see for example December 2017 and early January 2018 swarms; Fig. 5a,b and Supplementary Fig. S1) was expected to be triggered, but it did not occur simply because the flux of liquid water phase migrating upward in the shallow hydrothermal system lowered considerably as demonstrated by the subsequent net decrease of fumarolic fluxes and the drop in vent temperatures (Figs. 9,10). After the 16–17 April, the water was drained away, outside the dome, likely penetrating along the NW-SE regional structure further activated in late April 2018. Thus, pore pressure was released to areas away from the paths leading to the dome-hosted and steam-rich shallow hydrothermal system and to the summit fumarolic zone. Therefore, only gases, enriched in the "anomalous" magma-related component, could flow upward after separating from the deep hydrothermal system.
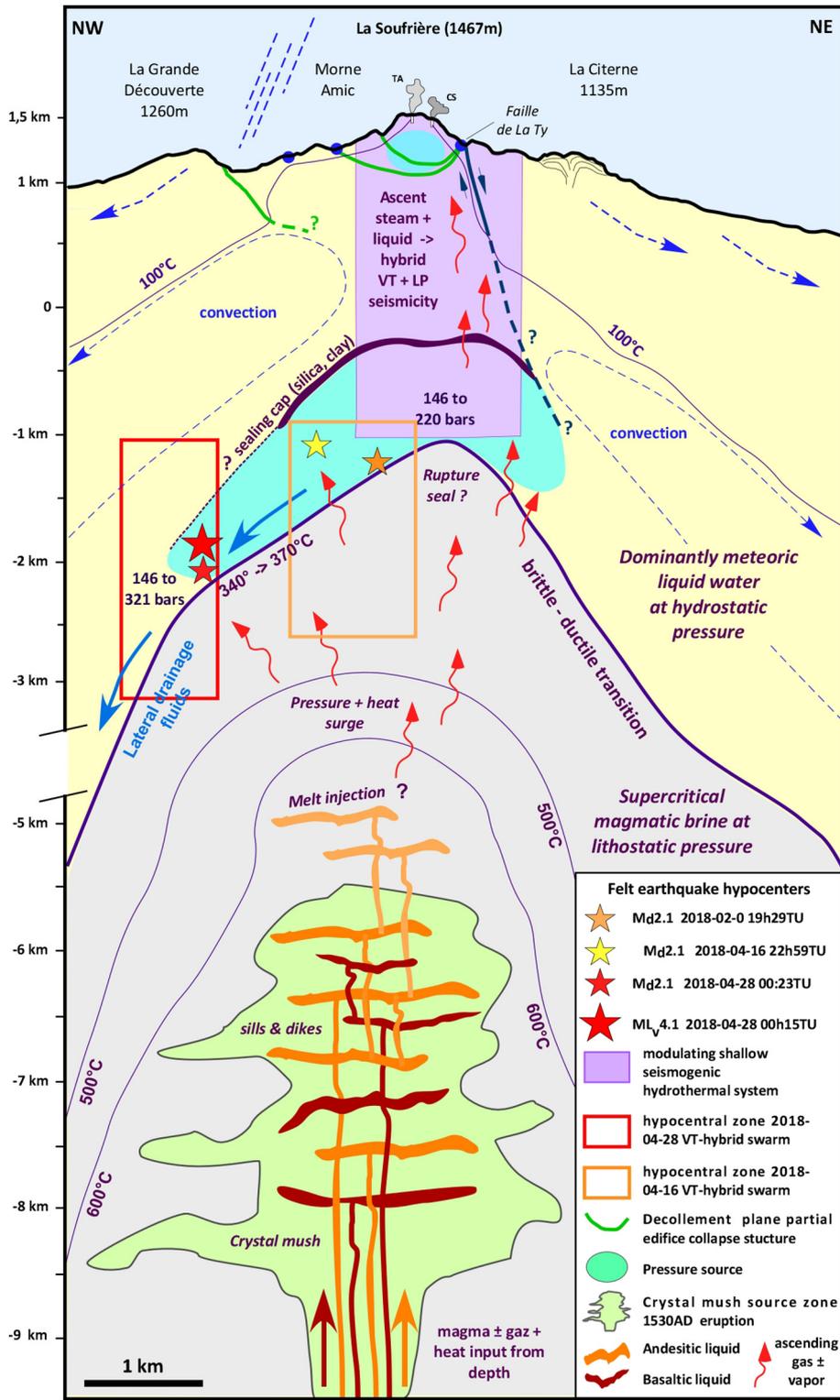
**Fig. 18.** Conceptual model of the La Soufrière of Guadeloupe and the February–April 2018 unrest episode. The conceptual model summarizes the evolution of observed geophysical and geochemical processes, including the build-up of pore pressures of thermal derivation.

Vapour separation, i.e. the mechanical decoupling of gas and liquid, oc-curs very likely when boiling water soon abandon undrained condi-tions, experiencing at depth a significant horizontal displacement (Arnorsson and Gunnlaugsson, 1985) due to deep lateral drainage out-side the dome, along the NW-SE fault segment that was seismically ac-tivated on 16–17 April 2018 (Fig. 18). This mechanism is testified for by the samples from 23 March 2018 to 2 June 2018 in Fig. 17, which plot following along the vapour separation curve at 300 °C and 80 bar. This

suggests that the vapour separation process was deeper - hence closer to the overpressure boiling source - than before 23 March and after 2 June.

Along the NW-SE fault structure, the same temperature rise (from 340 °C to the critical point, 374 °C, or from 613 K to 647 K) inferred from fumarolic fluid compositions (Fig. 17) determined a dramatic rise of overpressures. This can be estimated by considering the isochoric build-up of thermal pressure, that is, the fluid pressure increase caused

by heating a single finite fluid-filled pore volume (e.g., Delaney, 1982; Norton, 1984; Turcotte and Schubert, 1982; Ganguly, 2009):

$$\Delta P = \int_{613\,K}^{647\,K} \frac{a}{\beta} dT \qquad (6)$$

in which $\alpha$ is the isobaric thermal expansivity and $\beta$ is the isothermal compressibility, their ratio being unity at the water critical point because both parameters tend to converge. Given the T-dependence of the $\alpha/\beta$ ratio in the T-range of interest by fitting NIST steam tables (NIST, 2018), Eq. (6) gives an overpressure of 175 bar, that is, a pore pressure of 321 bar at the hypocenter of the 27 April, M 4.1, earthquake (2 km b.s.l. or 3.1 below the local ground-level; Fig. 18). This value is remarkably higher than the 220 bar inferred for an open system in which high-permeable fractures released the overpressure accumulated at 1 km b.s.l. (2.5 km depth below the volcano summit). These numbers are useful to give an idea of how the pore pressure increase along the same isotherm can affect rock behaviour. However, we cannot push further the argument as a precise treatment of thermoelastic effects and rock failure at the different sites would first demand the reconstruction of the local variations of the thermal field, and should include how fluid flow and resulting seepage forces modify the effective stresses (Barenblatt et al., 1960; Mourgues and Cobbold, 2003; Rozhko et al., 2007).

Nevertheless, given the current state of the dome, a thermally-driven build-up of overpressures comparable to the one reported in this study can lead to important rock failure and a phreatic eruption only when 1) self-sealing phenomena occur to confine fixed-fluid volumes, hence overpressure sources, sufficiently developed in the shallow hydrothermal system (rather than at 1 km b.s.l., i.e. 2.5 km below the summit), particularly in the sector currently responsible of measured deformations, and/or 2) the flow rate of the ascending hot fluids exceeds considerably both vertical and horizontal permeability-driven drainage through the deep dome fractures, thus impeding the pressure drop to nearly hydrostatic conditions. In this study we show evidence that this second scenario was initiated during the February-late April unrest phase, but could not reach its critical stage because water was effectively drained 2 km NW the dome axis through rock sectors of the NW-SE fault structure already solicited by the 16–17 swarm. This however produced 3 km NW away of the dome the $M_L$ 4.1 seismic episode, which is related to the sudden release of fluid overpressure initiating rock brecciation (Fournier, 2007; Sibson, 1986; Sillitoe, 2010) and can then be seen as a "failed phreatic" eruption.

As reported of the end of Section 4.2, one highly possible origin for the infiltration of deep magmatic gases is replenishment of the deep ($\geq 4.5$ km b.s.l.) magma chamber. In our view, the sudden 30 °C heating inferred from February to late April 2018 at depth > 0.5 km b.s.l. can only be achieved by the sudden arrival of a magma batch transferring its heat to the surrounding crustal fluids and triggering the thermoelastic effects that lead to undrained conditions (Delaney, 1982, 1984; McTigue, 1986), rapid overpressure build-up and rock failure. It is outside the scopes of the present study to provide a thorough treatment of this matter, which would also demand to account for the role played by tectonic stresses, but we can refer to the model developed by White and McCausland (2016) who have shown that distal volcano-tectonic (dVT) earthquakes are usually the earliest known precursor to eruptions at long dormant volcanoes. It is worth noting that the database in the work includes also the 1976 subsequent phreatic explosions of La Soufrière de Guadeloupe. The same may be said for the seismic swarms described here as dVT locations are disconnected spatially from the LP/hybrid (micro)seismicity beneath the volcano crater. The dVTs occur typically in swarm-like pulses of seismicity, characterized by large non-double component to the focal mechanism and with peaks in both event rate and average magnitude about the time of the initial (either magmatic or phreatic) activity. Coherent with the

observations reported in our study, swarm-like dVT seismicity ramps up in number and magnitude over weeks. As pulses of magma intrude, they gradually over-pressurize the aquifers and lubricate the local tectonically pre-stressed fault, allowing more and larger patches to slip (White and McCausland, 2016). We suggest that this activity may thus have peaked up with the 28 April M 4.1 earthquake although this initiated a typical main shock/aftershock swarm, rather than be the major event during a ramping up sequence, as in principles required for distal VT earthquakes swarms described by White and McCausland (2016). By using the Authors' relation cumulative seismic moment with the magma intruding volume ($Log_{10}V = 0.77xLog\Sigma M_0 - 5.32$, with volume V in cubic meters and moment $M_0$ in Nm; White and McCausland, 2016), we see that an intrusion of $2.7 \times 10^6$ m³, corresponding to a sphere of only 173 m in diameter, may have emplaced between February and late April 2018. Based on the sensitivity of our GPS network (Section 3.2.1) and in line with the physico-numerical findings in Coulon et al. (2017) on distal pressure changes triggering dVT seismicity, we conjecture that such a small intrusion might have emplaced well below the brittle-ductile transitions.

### 4.4. Lessons learnt: implications for volcanic surveillance and the monitoring strategy

Geophysical and geochemical data of this study show that a phreatic eruption at La Soufrière volcano did not occur during the 2018 unrest because of the high degree of fracturing and permeability of the volcanic dome, whose mechanical state has deeply changed after the 1976 eruption (Komorowski et al., 2005; Rosas-Carbajal et al., 2016). However, episode of deep magmatic degassing point to the likely replenishment of the magma storage zones. This increases the probability for a future eruption to start with a sudden phreato-magmatic phase anticipated by a very short-lived phreatic phase. For the very same reasons, seismic activities and unrest episodes like the one recorded in February–April 2018 must be seen on one side as failed phreatic eruptions, and on the other side as episodes prodromal to even major energy releases implying the destabilization of the hydrothermal system within the dome or the rise of magma batches.

The system has been evolving towards reactivation since 1992, as evidenced by geochemical data pointing to the 1976 (supercritical) cluster of points. The presence of acid species (HCl and $SO_2$) and the lack of important sealing, active in 1976, should not mask the arrival of deep magmatic gas inputs prior to any future eruption. However, we cannot yet exclude that this may be preceded by a short phase in which fumarole chemistry becomes more hydrothermal. This can be also suggested by the composition of gases discharged around 28 April 2018, in concomitance with the locking episode of summit fractures (Fig. 8). A similar, but far more important behaviour, was in fact observed at Galeras, because of pre-eruptive sealing phenomena (Brombach et al., 2000; Fischer et al., 1997). In the case of La Soufrière, sealing could lead to fluid accumulation and rapid pore pressure build up under undrained conditions, and destabilize the shallow hydrothermal pressure source, leading the system to explosive activity. In addition, it can also favor the sliding of the volcano south-west flank, subject to a basal gravitational spread, because of the reduction of the coefficient of friction and the increase of pore pressure along mechanically weak areas in the dome. A rapidly escalating unrest could in fact trigger slope instability and partial collapse of the south-western flank as suggested by Komorowski et al. (2005) and Rosas-Carbajal et al. (2016) and modelled by Peruzzetto et al. (2019).

This scenario and, particularly, the fact that we could not forecast the 227 April 2018 event (intended as a phreatic eruption) call upon the need for the in-situ high-frequency collection and full analysis of the fumarolic fluids, in order to track the short-lived P-T transients of the hydrothermal system (Barberi et al., 1992; Rouwet et al., 2014; Stix and de Moor, 2018). This strategy, elsewhere successfully implemented via in-situ mass spectrometry (e.g., Campi Flegrei; Fedele et al., 2017), at La

Soufrière presents many challenges related to intrinsic limits (high required power supply, instrumental fragility, costs and also logistics) and its hostile environment (rainy and windy conditions in a tropical environment, difficult accessibility, exposition to corrosion and unstable working conditions). At La Soufrière, it is however necessary to couple a full analysis including minor species (e.g., $H_2$, CO, $CH_4$, He) to the plume continuous measurements already operated via Multigas stations. Moreover, at La Soufrière Multigas sensors cannot provide the same levels of accuracy as at other volcanic sites where the sampled plumes emit superheated steam, much less affected by humidity than at La Soufrière (Aiuppa et al., 2011, 2018; De Moor et al., 2016).

In light of the strong role played by fluid release, hence by advective heat transport, it is then priority to improve our monitoring systems and surveillance protocols to 1) detect rapid hydrothermal transients in heat flux, 2) map and track variations in the distribution of deep isotherms. We want to stress here that joining thermal calculations based on energy conservation (e.g., Di Renzo et al., 2016; Moretti et al., 2018) to the deformation modeling adopted here would be a strict test for magma plumbing models as well as for sources responsible of observed rapid deformations, because they considerably narrow the domain of solutions to a set that are very similar (temporal similarity) and congruent (spatially similar). In this respect, a reasonable development of geothermal activity in the La Soufrière surroundings could represent a major contribution to track the evolution of deep temperatures, as well as anomalous chemical signatures of deep fluids. In addition, a detailed survey of spring water chemistry and isotope chemistry, extended to dissolved gases, will provide the necessary basis to model the chemical and hydraulic interaction between deep volcanic gases, the hydrothermal system and groundwaters, also contributing to the identification of possible high-pressure groundwater pathways.

On the geophysical side, the likely occurrence of rapid deformation pulses warns of the possibility of contamination of the broadband seismic signal due to tilt change, especially for long-period signals (Aoyama and Oshima, 2008; Pino et al., 2011), and suggests that effective tiltmetric measurements should be performed, also considering the role played by aseismic slip along the deep fractures cutting the dome. These should be accompanied by permanent gravity measurements, as well as dilatometric measurements (e.g., Scarpa et al., 2007), in order to track the evolution of the 6 km deep magma chamber and its refilling. These measurements would also help understanding better the mass transfer-stress-strain relationships occurring on La Soufrière and accompanying distal seismicity, which has the potential for estimating intrusive volumes and forecasting eruptions (White and McCausland, 2016; Coulon et al., 2017). Hence, future accurate assessments should also add to scrutiny the seismic swarms periodically occurring in the Les Saintes archipelago, located km SE of La Soufrière between the Guadeloupe and Dominica (see also Bazin et al., 2010; Feuillet et al., 2011 and references therein) and often characterized by important non-double component.

In light of the small volume of magma emplaced (see Section 4.3) and the short timescales between mafic recharge and eruption, which for the 1530 CE eruption span from tens of days to tens of hours (Pichavant et al., 2018), the improvement of the observatory capability to detect and interpret subtle variations related to the refilling of the 6–7 km deep magma chamber is obviously a major task. As shown here, as well as in other critical volcanic-hydrothermal areas (e.g. Campi Flegrei, Italy; Troise et al., 2019), such a task can be accomplished only through accurate joint consideration and analysis of geophysical and geochemical data (Supplementary Fig. S7 and Supplementary Table 1).

## 5. Conclusions

The La Soufrière of Guadeloupe unrest attained on 27 April 2018 its relative maximum since 42 years, i.e. after the 1976–1977 phreatic eruption. Recorded events include:

- 1 felt earthquake M 2.1 on 1 st February 2018 in a sequence of 30 earthquakes located at 1 km bsl (2.5 km depth below the volcano summit);
- 1 felt earthquake M 2.1 on 16–17 April in a sequence of 140 earthquakes located up to 1 km NW away of the dome, with most energetic events (M > 1) at a depth between 1 and 1.6 km bsl (2.5 and 3.1 km below the volcano summit);
- 2 felt earthquakes on April 27, including that of magnitude $M_L$ 4.1 in a sequence of 180 earthquakes located at about 2–3 km NW away from the dome, with most energetic events (M > 2) at a depth of 2 km bsl (3 km below the local ground-level).

This level of volcanic seismicity, unprecedented since 1976, has been associated with

1) a clearly magmatic signature of "pulses" of gases rich in $CO_2$, HCl, $H_2S$, and $SO_2$ in significant concentration around the vents;

2) the emission of hot hydrothermal fluids discharged by a hydrothermal system heated and pressurized ($\Delta P$ between 64 and 175 bar) from the deep areas of the volcanic system due to arrival of a major magmatic gas pulse;

3) horizontal deformation velocities around the dome (<1 km) up to 9 mm/year between 1995 and 2018 that are related to the shallow pressurization of the system hydrothermal as well as the gravitational spreading of the south-west flank of the dome.

4) renewed phases of fracture opening on the dome.

Geochemical analysis, and its thermodynamic interpretation, show that there has been a rise in fluids of deep origin (magmatic). This caused transient phases of overpressure and overheating at the base of the hydrothermal system, particularly in a source volume that we locate 2.5 km deep below the volcano summit. This excess fluid pressure was responsible for the 2018 considerable increase of volcanic seismicity on the Grande Découverte-Soufriere massif. The seismicity recorded along the NW-SE regional fault crossing the volcanic massif presents elements compatible with a process of hydrofracturing and/or hydroshearing. Nevertheless, at the scale of the dome, overpressure was dissipated either upward, through the highly permeable vertical fractures dissecting the dome, and laterally, by triggering slip along the NW-SE fault. This sequence of events preserved the stability of the shallow hydrothermal system, whose currently small pressure source at about 0.5 km depth is responsible for the radial component of the deformation observed at the summit.

Comparison of thermochemical features of current fumarolic discharges with 1997 and July 1976 data indicates that the hydrothermal system, reactivated since 1992, has increased its vigor, evolving from an early development phase dominated by important steam condensation (1997 data) to a mature condition in which boiling accompanies a clear increase of hydrothermal temperature, hence heat flux, and pressure, thus re-approaching the pre-1976 state.

Drainage of the hydrothermal liquid (water) outside the dome after the 16–17 April swarm along a NW-SE regional structure, inhibited the occurrence of a phreatic eruption which points to the conclusion that the 27 April $M_L$ 4.1 earthquake represents a failed phreatic eruption. No clear evidence can indicate so far the rise of magma to depths lower than those of the andesitic magma chamber (i.e. <6–7 km below the La Soufrière summit), although He-based chemical ratios and contrasting halogen behaviour have already suggested the occurrence of refreshment and/or replenishment of such a magma chamber. Based on distal seismicity evaluations, particularly the ramp up of magnitudes, a magmatic volume of $2.7 \times 10^6$ $m^3$ may have intruded between February and late April 2018.

The main lesson we have learnt from this record of events is that La Soufrière of Guadeloupe has changed behaviour and is at a significantly higher level of activity than it has been over the last 40 years. Given the increase in seismic and fumarolic activity recorded since February 2018, we cannot exclude an intensification of phenomena in the future, the present-day hydrothermal system being recharging in a P-T condition corresponding to the pre-1976 one, and not

dissimilar to Montserrat before the eruption that started in 1995 (Chiodini et al., 1996). Only a high-frequency joint geophysical, thermal and geochemical monitoring can disclose the rapid transient in pressure and temperature able to destabilize the hydrothermal system. Future eruptive activity may be preceded by a short phase in which fumarole chemistry becomes more hydrothermal due to sealing phenomena. This could bring to fluid accumulation and rapid pore pressure build-up destabilizing the shallow hydrothermal pressure source, leading to the (initial) phreatic explosion and favoring the sliding of the volcano south-west flank.

Supplementary data to this article can be found online at https://doi.org/10.1016/j.jvolgeores.2020.106769.

## CRediT authorship contribution statement

**Roberto Moretti:** Conceptualization, Investigation, Project administration, Formal analysis, Writing - original draft, Writing - review & editing, Supervision, Visualization, Data curation, Validation. **Jean-Christophe Komorowski:** Conceptualization, Project administration, Funding acquisition, Writing - review & editing, Supervision.**Guillaume Ucciani:** Formal analysis, Visualization, Investigation. **Séverine Moune:** Visualization, Data curation, Conceptualization, Investigation, Writing - review & editing. **David Jessop:** Formal analysis, Data curation, Conceptualization, Investigation, Writing - review & editing. **Jean-Bernard de Chabalier:** Formal analysis, Visualization, Data curation, Investigation. **François Beauducel:** Formal analysis, Software, Investigation, Visualization. **Magali Bonifacie:** Formal analysis, Investigation. **Arnaud Burtin:** Data curation, Validation. **Martin Vallée:** Formal analysis, Software, Visualization.**Sebastien Deroussi:** Resources, Data curation, Investigation, Validation. **Vincent Robert:** Resources, Formal analysis, Data curation, Validation. **Dominique Gibert:** Data curation, Validation. **Tristan Didier:** Resources, Data curation, Validation. **Thierry Kitou:** Resources, Data curation, Validation. **Nathalie Feuillet:** Conceptualization. **Patrick Allard:** Conceptualization, Writing - review & editing. **Giancarlo Tamburello:** Writing - review & editing. **Tara Shreve:** Writing - review & editing. **Jean-Marie Saurel:** Data curation, Validation. **Arnaud Lemarchand:** Funding acquisition, Data curation, Validation. **Marina Rosas-Carbajal:** Writing - review & editing. **Pierre Agrinier:** Formal analysis. **Anne Le Friant:** Project administration, Funding acquisition, Supervision. **Marc Chaussidon:** Project administration, Funding acquisition, Writing - review & editing, Supervision.

## Declaration of competing interest

The authors declare that they have no known competing financial interests or personal relationships that could have appeared to influence the work reported in this paper.

## Acknowledgements

## References

Aiuppa, A., Federico, C., Giudice, G., Gurrieri, S., 2005. Chemical mapping of a fumarolic field: la Fossa crater, Vulcano Island (Aeolian Islands, Italy). Geophys. Res. Lett. 32 (13).

Aiuppa, A., Shinohara, H., Tamburello, G., Giudice, G., Liuzzo, M., Moretti, R., 2011. Hydrogen in the gas plume of an open vent volcano (Mt. Etna, Italy). JOURNAL OF GEOPHYSICAL RESEARCH: SOLID EARTH 116, 1–5.

Aiuppa, A., de Moor, J.M., Arellano, S., Coppola, D., Francofonte, V., Galle, B., Giudice, G., Liuzzo, M., Mendoza, E., Saballos, A., Tamburello, G., Battaglia, A., Bitetto, M., Gurrieri, S., Laiolo, M., Mastrolia, A., Moretti, Roberto, 2018. Tracking formation of a lava lake from ground and space: Masaya volcano (Nicaragua), 2014–2017. Geochem. Geophys. Geosyst. 19 (2), 496–515.

Allard, P., 1983. The origin of hydrogen, carbon, Sulphur, nitrogen and rare gases in volcanic exhalations: Evidence from isotope geochemistry. Chapter 25. Forecasting Volcanic Events, pp. 337–386.

Allard, P., Hammouya, G., Parello, F., 1998. Diffuse magmatic soil degassing at Soufrière of Guadeloupe, Antilles. Comptes Rendus de l'Academie des Sciences Series IIA Earth and Planetary Science 5 (327), 315–318.

Allard, P., Aiuppa, A., Beauducel, F., Gaudin, D., Di Napoli, R., Calabrese, S., Parello, F., Crispi, O., Hammouya, G., Tamburello, G., 2014. Steam and gas emission rate from La Soufriere volcano, Guadeloupe (Lesser Antilles): implications for the magmatic supply during degassing unrest. Chem. Geol. 384, 76–93.

Aoyama, H., Oshima, H., 2008. Tilt change recorded by broadband seismometer prior to small phreatic explosion of Meakan-dake volcano, Hokkaido, Japan. Geophys. Res. Lett. 35 (6).

Arnorsson, S., Gunnlaugsson, E., 1985. New gas geothermometers for geothermal exploration - Calibration and application. Geochim. Cosmochim. Acta 49, 1307–1325.

Barberi, F., Bertagnini, A., Landi, P., Principe, C., 1992. A review on phreatic eruptions and their precursors. J. Volcanol. Geotherm. Res. 52 (4), 231–246.

Barenblatt, G.I., Zheltov, I.P., Kochina, I.N., 1960. Basic concepts in the theory of seepage of homogeneous liquids in fissured rocks. J. Appl. Math. Mech. 24, 1286–1303.

Barrabé, L., Jolivet, J., 1958. Les récentes manifestations d'activité de la Guadeloupe (Petites Antilles). (French) Recent activity manifestations of Guadeloupe (Lesser Antilles). Bull. Volcanol. 19, 143–157.

Battaglia, M., Troise, C., Obrizzo, F., Pingue, F., De Natale, G., 2006. Evidence for fluid migration as the source of deformation at Campi Flegrei caldera (Italy). Geophys. Res. Lett. 33 (1).

Bazin, S., Feuillet, N., Duclos, C., Crawford, W., Nercessian, A., Bengoubou-Valérius, M., Beauducel, F., Singh, S.C., 2010. The 2004–2005 Les Saintes (French West Indies) seismic aftershock sequence observed with ocean bottom seismometers. Tectonophysics 489 (1-4), 91–103.

Bigot, S., Boudon, G., Semet, M.P., Hammouya, G., 1994. Traçage chimique de la circulation des eaux souterraines sur le volcan de la Grande Découverte (la Soufriére), Guadeloupe. CR Acad. Sci. Paris 318, 1215–1221.

Boichu, M., Villemant, B., Boudon, G., 2008. A model for episodic degassing of an andesitic magma intrusion. Journal of Geophysical Research: Solid Earth 113 (B7).

Boichu, M., Villemant, B., Boudon, G., 2011. Degassing at La Soufrière de Guadeloupe volcano (Lesser Antilles) since the last eruptive crisis in 1975{77}: result of a shallow magma intrusion? J. Volcanol. Geotherm. Res. 203, 102{112.

Brodsky, E.E., Sturtevant, B., Kanamori, H., 1998. Earthquakes, volcanoes, and rectified diffusion. Journal of Geophysical Research: Solid Earth 103 (B10), 23827–23838.

Brombach, T., Marini, L., Hunziker, J.C., 2000. Geochemistry of the thermal springs and fumaroles of Basse-Terre Island, Guadeloupe, Lesser Antilles. Bull. Volcanol. 61 (7), 477–490.

Brothelande, E., Finizola, A., Peltier, A., Delcher, E., Komorowski, J.C., Di Gangi, F., Borgogno, G., Passarella, M., Trovato, C., Legendre, Y., 2014. Fluid circulation pattern inside La Soufrière volcano (Guadeloupe) inferred from combined electrical resistivity tomography, self-potential, soil temperature and diffuse degassing measurements. J. Volcanol. Geotherm. Res. 288, 105–122.

Boudon, G., Dagain, J., Semet, M.P., Westercamp, D., 1988. Notice explicative de la carte géologique au 1/20.000 ème du massif volcanique de la Soufrière (Département de la Guadeloupe, Petites Antilles). BRGM, CNRS, DRM, IPGP, Paris 43 pp.

Boudon, G., Komorowski, J.C., Villemant, B., Semet, M.P., 2008. A new scenario for the last magmatic eruption of La Soufrière of Guadeloupe (Lesser Antilles) in 1530 AD Evidence from stratigraphy radiocarbon dating and magmatic evolution of erupted products. J. Volcanol. Geotherm. Res. 178 (3), 474–490.

Buck, W.R., Martinez, F., Steckler, M.S., Cochran, J.R., 1988. Thermal consequences of lithospheric extension: pure and simple. Tectonics 7 (2), 213–234.

Caliro, S., Chiodini, G., Paonita, A., 2014. Geochemical evidences of magma dynamics at Campi Flegrei (Italy). Geochim. Cosmochim. Acta 132, 1–15.

Chatterjee, S.N., Pitt, A.M., Iyer, H.M., 1985. Vp/Vs ratios in the Yellowstone national park region, Wyoming. J. Volcanol. Geotherm. Res. 26, 213–230.

Chevrier, R.M., Dajlevic, D., Le Guern, F., Rouyerr, J.L., 1976. Données recueillies sur la phase gazeuse de la Soufière (Guadeloupe) du 13 Juillet au 20 Septembre 1976. Rapport CEA, Départment de protection, Novembre 1976.

Chiodini, G., 2009. CO2/CH4 ratio in fumaroles a powerful tool to detect magma degassing episodes at quiescent volcanoes. Geophys. Res. Lett. 36 (2).

Chiodini, G., Marini, L., 1998. Hydrothermal gas equilibria: the H2O-H2-CO2-CO-CH4 system. Geochim. Cosmochim. Acta 62 (15), 2673–2687.

Chiodini, G., Cioni, R., Frullani, A., Guidi, M., Marini, L., Prati, F., Raco, B., 1996. Fluid geochemistry of Montserrat Island, West Indies. Bull. Volcanol. 58 (5), 380–392.

Chiodini, G., Marini, L., Russo, M., 2001. Geochemical evidence for the existence of high-temperature hydrothermal brines at Vesuvio volcano, Italy. Geochim. Cosmochim. Acta 65 (13), 2129–2147.

Chiodini, G., Vandemeulebrouck, J., Caliro, S., D'Auria, L., De Martino, P., Mangiacapra, A., Petrillo, Z., 2015. Evidence of thermal-driven processes triggering the 2005–2014 unrest at Campi Flegrei caldera. Earth Planet. Sci. Lett. 414, 58–67.

Collettini, C., Barchi, M.R., 2002. A low-angle normal fault in the Umbria region (Central Italy): a mechanical model for the related microseismicity. Tectonophysics 359 (1–2), 97–115.

Connolly, J.A.D., 1997. Devolatilization-generated fluid pressure and deformation-propagated fluid flow during prograde regional metamorphism. J. Geophys. Res. 102 (B8), 18149–18173.

Coulon, C.A., Hsieh, P.A., White, R., Lowenstern, J.B., Ingebritsen, S.E., 2017. Causes of distal volcano-tectonic seismicity inferred from hydrothermal modelling. J. Volcanol. Geotherm. Res. 345, 98–108.

Cox, S.F., 1995. Faulting processes at high fluid pressures: an example of fault valve behavior from the Wattle Gully Fault, Victoria, Australia. Journal of Geophysical Research (Solid Earth) 100, 12,841–12,859. https://doi.org/10.1029/95JB00915.

D'Amore, F., Panichi, C., 1980. Evaluation of deep temperatures of hydrothermal systems by a new gas geothermometer. Geochim. Cosmochim. Acta 44 (3), 549–556.

de Moor, J.M., Aiuppa, A., Avard, G., Wehrmann, H., Dunbar, N., Muller, C., Tamburello, G., Giudice, G., Liuzzo, M.Moretti, 2016. Turmoil at Turrialba Volcano (Costa Rica): Degassing and eruptive processes inferred from high-frequency gas monitoring. J. Geophys. Res. Solid Earth 121 (8), 5761–5775.

Del Pezzo, E., Bianco, F., Saccorotti, G., 2004. Seismic source dynamics at Vesuvius volcano, Italy. J. Volcanol. Geotherm. Res. 133 (1–4), 23–39.

Delaney, P.T., 1982. Rpid intrusion of magma into wet rock: groundwater flow due to pore pressure increases. J. Geophys. Res. 87, 7739–7756.

Delaney, P., 1984. Heating of a fully saturated Darcian half-space: pressure generation fluid expulsion and phase change. Int. J. Heat Mass Transf. 27, 1327–1335.

Di Renzo, V., Wohletz, K., Civetta, L., Moretti, R., Orsi, G., Gasparini, P., 2016. The thermal regime of the Campi Flegrei magmatic system reconstructed through 3D numerical simulations. J. Volcanol. Geotherm. Res. 328, 210–221.

Dorel, J., Eschenbrenner, S., Feuillard, M., 1979. Coupes sismiques des structures superficielles dans les petites antilles—I: Guadeloupe. Pure Appl. Geophys. 117 (9), 1050–1069.

Fabre, R., Chaigneau, M., 1960. Technique de prélèvement et d'analyse de gaz de fumerolles de volcans. Exemples d'analyses de gaz prélevés à la montagne Pelée (Martinique) et à la Grande Soufrière (Guadeloupe). Bull. Volcanol. 23 (1), 21–30.

Fedele, A., Pedone, M., Moretti, R., Wiersberg, T., Somma, R., Troise, C., De Natale, G., 2017. Real-time quadrupole mass spectrometry of hydrothermal gases from the unstable Pisciarelli fumaroles (Campi Flegrei): trends, challenges and processes. Int. J. Mass Spectrom. 415, 44–54.

Feuillard, M., et al., 1983. The 1975-1977 crisis of La Soufrière de Guadeloupe (FWI): a still-born magmatic eruption. J. Volcanol. Geotherm. Res. 16, 317{334.

Feuillard, M., 2011. In: Jasor, Pointe-à-Pitre (Ed.), La Soufrière de la Guadeloupe : un volcan et un peuple pp 246.

Feuillet, N., Manighetti, I., Tapponnier, P., Jacques, E., 2002. Arc parallel extension and localization of volcanic complexes in Guadeloupe, Lesser Antilles. Journal of Geophysical Research: Solid Earth 107 (B12), ETG 3–1ETG 3-29 107.B12.

Feuillet, N., Beauducel, F., Tapponnier, P., 2011. Tectonic context of moderate to large historical earthquakes in the lesser antilles and mechanical coupling with volcanoes. Journal of Geophysical Research: Solid Earth 1978 (2012), 116.

Fischer, T.P., Sturchio, N.C., Stix, J., Arehart, G.B., Counce, D., Williams, S.N., 1997. The chemical and isotopic composition of fumarolic gases and spring discharges from Galeras Volcano, Colombia. J. Volcanol. Geotherm. Res. 77 (1–4), 229–253.

Fournier, R.O., 2007. Hydrothermal systems and volcano geochemistry. Volcano deformation. Springer, Berlin, Heidelberg, pp. 323–341.

Ganguly, J., 2009. Thermodynamics in Earth and Planetary Sciences. Springer Science & Business Media.

Gaudin, D., Beauducel, F., Coutant, O., Delacourt, C., Richon, P., de Chabalier, J.B., Hammouya, G., 2016. Mass and heat flux balance of La Soufrière volcano (Guadeloupe) from aerial infrared thermal imaging. J. Volcanol. Geotherm. Res. 320, 107–116.

Giggenbach, W.F., 1980. Geothermal gas equilibria. Geochim. Cosmochim. Acta 44 (12), 2021–2032.

Giggenbach, W., 1987. Redox processes governing the chemistry of fumarolic gas discharges from White Island, New Zealand. Appl. Geochem. 2, 143–161.

Giggenbach, W.F., 1988. Geothermal solute equilibria. Derivation of Na-K-Mg-Ca geoindicators. Geochim. Cosmochim. Acta 52, 2749–2765.

Giggenbach, W.F., 1997. The origin and evolution of fluids in magmatic-hydrothermal systems. In: Barnes, H.L. (Ed.), Geochemistry of Hydrothermal Ore Deposits, 3rd edition John Wiley & Sons, New York, pp. 737–796.

Giggenbach, W.F., Goguel, R.L., 1989. Collection and Analysis of Geothermal and Volcanic Water and Gas Discharges. Report No. CD 2401. Department of Scientific and Industrial Research. Chemistry Division, Petone, New Zealand.

Haimson, B.C., Zhao, Z., 1991. Effect of borehole size and pressurization rate on hydraulic fracturing breakdown pressure. The 32nd US Symposium on Rock Mechanics (USRMS). American Rock Mechanics Association.

Hanks, T.C., Kanamori, H., 1979. A moment magnitude scale. J. Geophys. Res. 84 (B5), 2348–2350.

Hapel-Lachênaie, T., Peyre, A., Fontelliau, C., 1798. Rapport fait aux citoyens Victor Hugues et Lebas, agents particuliers du directoire exécutif aux isles du vent, par la commission établie en vertu de leur arrété du 12 vendémiaire, an 6 de la république, pour examiner la situation du Volcan de la Guadeloupe, et les effets de l'éruption qui a eu lieu dans la nuit du 7 au 8 du même mois. An VI. Facsimile, Société d'Histoire De la Guadeloupe, Basse-Terre, p. 179.

Harris, A., 2013. Thermal Remote Sensing of Active Volcanoes: A user's Manual. Cambridge University Press (728 pp).

Hill, D.P., Ellsworth, W.L., Johnston, M.J.S., Langbein, J.O., Oppenheimer, D.H., Pitt, A.M., Reasenberg, P.A., Sorey, M.L., McNutt, S.R., 1990. The 1989 earthquake swarm beneath Mammoth Mountain, California: an initial look at the 4 May through 30 September activity. Bull. Seismol. Soc. Am. 80 (2), 325–339.

Hill, D.P., Pollitz, F., Newhall, C., 2002. Earthquake-volcano interactions. Phys. Today 55 (11), 41–47.

Hincks, T.K., Komorowski, J.-C., Sparks, S.R., Aspinall, W.P., 2014. Retrospective analysis of uncertain eruption precursors at La Soufriere volcano, Guadeloupe, 1975{77}: volcanic hazard assessment using a bayesian belief network approach. J. Appl. Volcanol. 3 (1), 26.

Ito, H., DeVilbiss, J., Nur, A., 1979. Compressional and shear waves in saturated rock during water-steam transition. J. Geophys. Res. 84, 4731–4735.

Jean-Baptiste, P., Allard, P., Fourré, E., Parello, F., Aiuppa, A., 2014. Helium isotope systematics of volcanic gases and thermal waters of Guadeloupe Island, Lesser Antilles. J. Volcanol. Geotherm. Res. 283, 66–72.

Jolivet, J., 1958. La crise volcanique de 1956 à la Soufrière de la Guadeloupe. (French). The volcanic crisis of 1956 at La Soufrière of Guadeloupe. Annales de Géeophysique. vol. 14, p. 305.

Kehle, R., 1964. The determination of tectonic stresses through analysis of hydraulic well fracturing. J. Geophys. Res. Q 259–273.

Komorowski, J.-C., et al., 2001. L'activité éruptive et non-éruptive de la Soufrière de Guadeloupe: problèmes et implications de la phénoménologie et des signaux actuellement enregistrés. (French). Eruptive and non-eruptive activity from the Soufrière of Guadeloupe: problems and implications posed by the current phenomenology and monitoring signals. Workshop on volcanic hazards - Lesser Antilles volcanoes: from processes to signals. 18. PNRN (CNRS){INSU, BRGM, CEA, CEMAGREF, CNES, IRD, p. 19.

Komorowski, J.-C., et al., 2005. Guadeloupe. Volcanic Atlas of the Lesser Antilles. 65. Seismic Research Unit, The University of the West Indies Trinidad, p. 102.

Komorowski, J.-C., Legendre, Y., Caron, B., Boudon, G., 2008. Reconstruction and analysis of subplinian tephra dispersal during the 1530 AD Soufriere (Guadeloupe) eruption: Implications for scenario definition and hazards assessment. J. Volcanol. Geotherm. Res. 178, 491{515.

Komorowski, J.-C., Legendre, Y., Barsotti, S., Esposti Ongaro, T., Jenkins, S., Baxter, P., Boudon, G., Leone, F., Neri, A., Spence, R., Aspinall, W., Grancher, D., Redon, M., Chopineau, C., de Chabalier, J.-B., 2013. Assessing long term hazards for the Soufriere of Guadeloupe volcano: insights from a new eruptive chronology, credible scenario definition, and integrated impact modelling. International Association of Volcanology and Chemistry of the Earth's Interior (IAVCEI), Scientific Assembly, Kagoshima, Japan 19-24 Juy 2013, abstract, 4W_4D-P1, poster.

Komorowski, J., Hincks, T., Sparks, R., Aspinall, W., et al., 2015. Improving crisis decision-making at times of uncertain volcanic unrest (Guadeloupe, 1976). Global Volcanic Hazards and Risk. Cambridge University Press, p. 255.

Le Guern, F., Bernard, A., Chevrier, R., 1980. Soufrière of Guadeloupe 1976-1977 eruption. Mass and energy transfer and volcanic health hazards. Bull. Volcanol. 43, 577–593.

Legendre, Y., 2012. Reconstruction de l'histoire éruptive et scenarii éruptifs à La Soufrière de Guadeloupe: vers un modèle intégrale de fonctionnement du volcan. (French) [A high resolution reconstruction of the eruptive past and definition of eruptive scenarii at La Soufrière de Guadeloupe]. Ph.D. thesis, Paris. p. 7.

Lesparre, N., Gibert, D., Marteau, J., Komorowski, J.-C., Nicollin, F., Coutant, O., 2012. Density Muon Radiography of Soufrière of Guadeloupe Volcano: Comparison with Geological, Electrical Resistivity and Gravity data. Geophys. J. Int. https://doi.org/10.1111/j.1365-246X.2012.05546.x.

Lherminier, F., 1837a. Sur les produits du volcan de la Guadeloupe. Comptes rendus de l'Académie des sciences 454–455.

Lherminier, F., 1837b. L'eruption du volcan de la Guadeloupe. La Soufrière of Guadeloupe. Nouvelles Annales de Voyage 74, 349–350.

Lherminier, F., 1837c. Note sur l'eruption du volcan de la Guadeloupe. (French). On the products from the volcano of La Guadeloupe. Comptes rendus de l'Acađemie des sciences 294.

Lherminier, F., 1815. Réflexions sur les volcans, considérations sur la Guadeloupe. J. Phys. 80, 260–271.

Linde, A.T., Sacks, I.S., 1998. Triggering of volcanic eruptions. Nature 395 (6705), 888.

Lomax, A., Virieux, J., Volant, P., Berge-Thierry, C., 2000. Probabilistic earthquake location in 3D and layered models – introduction of a Metropolis-Gibbs method and comparison with linear locations. Advances in Seismic Event Location, pp. 101–134.

Marzocchi, W., 2002. Remote seismic influence on large explosive eruptions. Journal of Geophysical Research: Solid Earth 107 (B1).

Mastin, L.G., 1995. The thermodynamics of steam-blast eruptions. Bull. Volcanol. 57, 85–98.

McTigue, D.F., 1986. Thermoelastic response of fluid-saturated porous rock. Journal of Geophysical Research: Solid Earth 91 (B9), 9533–9542.

Micklethwaite, S., Cox, S.F., 2006. Progressive fault triggering and fluid flow in aftershock domains: examples from mineralized Archaean fault systems. Earth Planet. Sci. Lett. 250 (1–2), 318–330.

Miller, S.A., 2015. Modeling enhanced geothermal systems and the essential nature of large-scale changes in permeability at the onset of slip. Geofluids 15, 338–349.

Miller, S.A., Nur, A., 2000. Permeability as a toggle switch in £uid-controlled crustal processes. Earth Planet. Sci. Lett. 183 (2000), 133–146.

Miller, S.A., Nur, A., Olgaard, D.A., 1996. Earthquakes as a coupled shear stress - high pore pressure dynamical system. Geophys. Res. Lett. 23 (2), 197–200 JANUARY 15.

Miller, V., Voight, B., Ammon, C.J., Shalev, E., Thompson, G., 2010. Seismic expression of magma-induced crustal strains and localized fluid pressures during initial eruptive stages, Soufrière Hills Volcano, Montserrat. Geophys. Res. Lett. 37, L00E21. https://doi.org/10.1029/2010GL043997.

Mizutani, Y., Sugiura, T., 1982. Variations in chemical and isotopic compositions of fumarolic gases from Showashinzan volcano, Hokkaido, Japan. Geochem. J. 16 (2), 63–71.

Moretti, R., Papale, P., Ottonello, G., 2003. A model for the saturation of COHS fluids in silicate melts. Geol. Soc. Lond., Spec. Publ. 213 (1), 81–101.

Moretti, R., Arienzo, I., Civetta, L., Orsi, G., Papale, P., 2013a. Multiple magma degassing sources at an explosive volcano. Earth Planet. Sci. Lett. 367, 95–104.

Moretti, R., Arienzo, I., Orsi, G., Civetta, L., D'antonio, M., 2013b. The deep plumbing system of Ischia: a physico-chemical window on the fluid-saturated and CO2-sustained Neapolitan Volcanism (Southern Italy). J. Petrol. 54 (5), 951–984.

Moretti, R., De Natale, G., Troise, C., 2017. A geochemical and geophysical reappraisal to the significance of the recent unrest at Campi Flegrei caldera (Southern Italy). Geochem. Geophys. Geosyst. 18 (3), 1244–1269.

Moretti, R., Troise, C., Sarno, F., De Natale, G., 2018. Caldera unrest driven by CO 2-induced drying of the deep hydrothermal system. Sci. Rep. 8 (1), 8309.

Moretti, R., Arienzo, I., Di Renzo, V., Orsi, G., Arzilli, F., Brun, F., ... Deloule, E., 2019. Volatile segregation and generation of highly vesiculated explosive magmas by volatile-melt fining processes: The case of the Campanian Ignimbrite eruption. Chemical Geology 503, 1–14.

Mourgues, R., Cobbold, P.R., 2003. Some tectonic consequences of fluid overpressures and seepage forces as demonstrated by sandbox modelling. Tectonophysics 376 (1–2), 75–97.

Nakajima, J., Matsuzawa, T., Hasegawa, A., Zhao, D., 2001. Three-dimensional structure of Vp, Vs and Vp/Vs beneath northeastern Japan: Implications for arc magmatism and fluids. Journal of Geophysical Research: Solid Earth 106 (B10), 21843–21857.

Nakamura, K., 1977. Volcanoes as possible indicators of tectonic stress orientation–principle and proposal. J. Volcanol. and Geotherm. Res. 1–16.

Nicollin, F., Gibert, D., Beauducel, F., Boudon, G., Komorowski, J.-C., 2006. Electrical tomography of La Soufrière of Guadeloupe Volcano: field experiments, 1D inversion and qualitative interpretation. Earth Planet. Sci. Lett. 244, 709–724.

NIST, 2018. Thermophysical properties of fluid systems. NIST Chemistry WebBook, SRD 69. National Institute of Standards and Technology. U.S.Department of Commercehttps://webbook.nist.gov/chemistry/fluid/.

Norton, D.L., 1984. Theory of hydrothermal systems. Annu. Rev. Earth Planet. Sci. 12 (1), 155–177.

Norton, D., Knight, J., 1977. Transport phenomena in hydrothermal systems: cooling plutons. Am. J. Sci. 277.

Nostro, C., Stein, R.S., Cocco, M., Belardinelli, M.E., Marzocchi, W., 1998. Two-way coupling between Vesuvius eruptions and southern Apennine earthquakes, Italy, by elastic stress transfer. Journal of Geophysical Research: Solid Earth 103 (B10), 24487–24504.

Nuccio, P.M., Paonita, A., 2000. Investigation of the noble gas solubility in $H_2O$–$CO_2$ bearing silicate liquids at moderate pressure II: the extended ionic porosity (EIP) model. Earth Planet. Sci. Lett. 183 (3–4), 499–512.

Nugraha, A.D., Indrastuti, N., Kristianto, Gunawan, H., McCausland, W., Aulia, A.N., Harlianti, U., 2019. Joint 3-D tomographic imaging of Vp, Vs and Vp/Vs and hypocenter relocation at Sinabung volcano, Indonesia from November to December 2013. J. Volcanol. Geotherm. Res. 382, 210–223.

OVSG-IPGP, 1999-2019. Monthly reports on the activity of La Soufrière de Guadeloupe and on regional seismicity. http://www.ipgp.fr/ovsg/bulletins-mensuels-de-lovsg.

OVSG-IPGP, 2017. September 2017 monthly report. http://www.ipgp.fr/sites/default/files/ovsg_2017_bilan-annuel.pdf.

OVSG-IPGP, 2018a. seismic report. http://volcano.ipgp.jussieu.fr/guadeloupe/Communiques/2018/OVSG_20180202_SequenceSeismesVolcaniques_Soufri%C3%A8re.pdf.

OVSG-IPGP, 2018b. seismic report. http://volcano.ipgp.jussieu.fr/guadeloupe/Communiques/2018/OVSG_20180416_SequenceSeismesVolcaniques_Soufrie%CC%80re.pdf.

OVSG-IPGP, 2018c. seismic report seismic report. http://volcano.ipgp.jussieu.fr/guadeloupe/Communiques/2018/OVSG_20180428_SequenceSeismesSoufrier.pdf.

Peruzzetto, M., Komorowski, J.C., Le Friant, A., Rosas-Carbajal, M., Mangeney, A., Legendre, Y., 2019. Modeling of partial dome collapse of La Soufrière of Guadeloupe volcano: implications for hazard assessment and monitoring. Sci. Rep. 9 (1), 1–15.

Peyssonnel, J.A., Maty, M., 1756. Observations made upon the Brimstone-Hill (in French La Souffriere) in the Island of Guadelupa; by John Andrew Peyssonel, M. D. Member of the Royal Academies of Sciences of Paris and Montpelier, and of Marseilles and Rouen; the King of France's physician and Botanist Heretofore on the Coast of Barbary, and now in the Island of Guadelupa, F. R. S. Translated from the French by M. Maty, M. D. and F. R. S. Philos. Trans. 49, 564–579.

Pichavant, M., Poussineau, S., Lesne, P., Solaro, C., Bourdier, J.L., 2018. Experimental parametrization of magma mixing: application to the ad 1530 eruption of La Soufrière, Guadeloupe (Lesser Antilles). J. Petrol. 59 (2), 257–282.

Pino, N.A., Moretti, R., Allard, P., Boschi, E., 2011. Seismic precursors of a basaltic paroxysmal explosion track deep gas accumulation and slug upraise. Journal of Geophysical Research: Solid Earth 116 (B2).

Poussineau, S., 2005. Dynamique des magmas andésitiques: approche expérimentale et pétrostructurale; application à la Soufrière de Guadeloupe et à la Montagne Pelée. Doctoral dissertation. Université d'Orléans.

Pritchard, M.E., Mather, T.A., McNutt, S.R., Delgado, F.J., Reath, K., 2019. Thoughts on the criteria to determine the origin of volcanic unrest as magmatic or non-magmatic. Phil. Trans. R. Soc. A 377 (2139), 20180008.

Reed, M.H., 1997. Hydrothermal alteration and its relationship to ore fluid composition. In: Barnes, H.L. (Ed.), Geochemistry of Hydrothermal Ore Deposits, 3rd edition John Wiley & Sons, New York, pp. 517–611.

Rosas-Carbajal, M., Komorowski, J.C., Nicollin, F., Gibert, D., 2016. Volcano electrical tomography unveils edifice collapse hazard linked to hydrothermal system structure and dynamics. Sci. Rep. 6, 29899.

Rouwet, D., Sandri, L., Marzocchi, W., Gottsmann, J., Selva, J., Tonini, R., Papale, P., 2014. Recognizing and tracking volcanic hazards related to non-magmatic unrest: a review. J. Appl. Volcanol. 3 (1), 17.

Rozhko, A.Y., Podladchikov, Y.Y., Renard, F., 2007. Failure patterns caused by localized rise in pore-fluid overpressure and effective strength of rocks. Geophys. Res. Lett. 34 (22).

Ruzié, L., Moreira, M., Crispi, O., 2012. Noble gas isotopes in hydrothermal volcanic fluids of La Soufrière volcano, Guadeloupe, Lesser Antilles arc. Chem. Geol. 304, 158–165.

Ruzié, L., Aubaud, C., Moreira, M., Agrinier, P., Dessert, C., Gréau, C., Crispi, O., 2013. Carbon and helium isotopes in thermal springs of La Soufrière volcano (Guadeloupe, Lesser Antilles): implications for volcanological monitoring. Chem. Geol. 359, 70–80.

Salaün, A., Villemant, B., Gérard, M., Komorowski, J.-C., Michel, A., 2011. Hydrothermal alteration in andesitic Volcanoes: Trace element redistribution in active and ancient hydrothermal systems of Guadeloupe (Lesser Antilles). J Geochem Expl 111, 59–83.

Sanders, C.O., Ponko, S.C., Nixon, L.D., Schwartz, E.A., 1995. Seismological evidence for magmatic and hydrothermal structure in Long Valley caldera from local earthquake attenuation and velocity tomography. Journal of Geophysical Research: Solid Earth 100 (B5), 8311–8326.

Scarpa, R., Amoruso, A., Crescentini, L., Romano, P., De Cesare, W., Martini, M., Scarpato, G., Linde, A.T., Sacks, S.I., 2007. New borehole strain system detects uplift at Campi Flegrei. Eos Trans. AGU 88 (18). https://doi.org/10.1029/2007EO180002.

Schmitt, D.R., Zoback, M.D., 1992. Diminished pore pressure in low-porosity crystalline rock under tensional failure: Apparent strengthening by dilatancy. Journal of Geophysical Research: Solid Earth 97 (B1), 273–288.

Semet, M.P., Vatin-Perignon, N., Vincent, P.M., Joron, J.L., 1982. Magma mixing once more: its involvement in triggering the 16th century volcanic activity at La Soufrière, Guadeloupe (FWI). Bull. PIRPSEV 60, 63.

Sheridan, M.F., 1980. Pyroclastic block flow from the September, 1976, eruption of La Soufrière volcano, Guadeloupe. Bull. Volcanol. 43 (2), 397–402.

Shinohara, H., 2005. A new technique to estimate volcanic gas composition: plume measurements with a portable multi-sensor system. J. Volcanol. Geotherm. Res. 143 (4), 319–333.

Sibson, R.H., 1986. Brecciation processes in fault zones: Inferences from earthquake rupturing. PAGEOPH 124, 159–175. https://doi.org/10.1007/BF00875724.

Sibson, R.H., 1990. Rupture nucleation on unfavorably oriented faults. Bull. Seismol. Soc. Am. 80, 1580–1604.

Sibson, R.H., 2000. Fluid involvement in normal faulting. J. Geodyn. 29, 469–499. https://doi.org/10.1016/S0264-3707(99)00042-3.

Sigurdsson, H., Houghton, B., McNutt, S., Rymer, H., Stix, J. (Eds.), 2015. The Encyclopedia of Volcanoes. Elsevier (1456 pp).

Sillitoe, R.H., 2010. Porphyry copper systems. Econ. Geol. 105 (1), 3–41.

Spencer Jr., J.W., Nur, A., 1976. The effects of pressure, temperature and pore water on velocities in westerly granite. J. Geophys. Res. 81, 899–904.

Stix, J., de Moor, J.M., 2018. Understanding and forecasting phreatic eruptions driven by magmatic degassing. Earth, Planets and Space 70 (1), 83.

Tamburello, G., Moune, S., Allard, P., Venugopal, S., Robert, V., Rosas-Carbajal, M., Ucciani, G., Deroussi, S., Kitou, T., Didier, T., Komorowski, J.-C., Beauducel, F., de Chabalier, J.-B., Lemarchand, A., Dessert, C., Moretti, R., 2019. Spatio-temporal relationships between fumarolic activity, hydrothermal fluidcirculation and geophysical signals at an arc volcano in degassing unrest: LaSoufrière of Guadeloupe (French West Indies). Geosciences 9 (11), 480.

Terakawa, T., Zoporowski, A., Galvan, B., Miller, S.A., 2010. High-pressure fl uid at hypocentral depths in the L'Aquila region inferred from earthquake focal mechanisms earthquake focal mechanisms. Geology 38 (11), 995–998. https://doi.org/10.1130/G31457.1 November 2010.

Touboul, M., Bourdon, B., Villemant, B., Boudon, G., Joron, J.L., 2007. 238 U–230 Th–226 Ra disequilibria in andesitic lavas of the last magmatic eruption of Guadeloupe Soufriere, French Antilles: processes and timescales of magma differentiation. Chem. Geol. 246 (3), 181–206.

Troise, C., 2001. Stress changes associated with volcanic sources: constraints on Kilauea rift dynamics. J.Volcanol.Geoth.Res. 109, 191–203.

Troise, C., De Natale, G., Schiavone, R., Somma, R., Moretti, R., 2019. The Campi Flegrei caldera unrest: discriminating magma intrusions from hydrothermal effects and implications for possible evolution. Earth Sci. Rev. 188, 108–122.

Turcotte, D.L., Schubert, G., 1982. Geodynamics: Applications of Continuum Physics to Geological Problems. 450 pp. John Wiley, New York.

Ucciani, G., 2015. Caractérisation spatiale et temporelle de la sismicité volcanique de la Soufrière de Guadeloupe: relation avec le système hydrothermal. Doctoral dissertation. Sorbonne Paris Cité.

Ucciani, G., Beauducel, F., Bouin, M.P., Nercessian, A., 2015. Dynamic of the volcanic activity of La Soufrière volcano (Guadeloupe, Lesser Antillles): Evidence for shallow fluid seismic sources. AGU Fall Meeting Abstracts.

Ventura, G., Vilardo, G., 1999. Seismic-based estimate of hydraulic parameters at Vesuvius Volcano. Geophys. Res. Lett. 26 (7), 887–890.

Villemant, B., et al., 2005. The memory of volcanic waters: shallow magma degassing revealed by halogen monitoring in thermal springs of La Soufrière volcano (Guadeloupe, Lesser Antilles). Earth Planet. Sci. Lett. 237, 710{728}.

Villemant, B., et al., 2014. Evidence for a new shallow magma intrusion at La Soufriere of Guadeloupe (Lesser Antilles): insights from long-term geochemical monitoring of halogen-rich hydrothermal fluids. J. Volcanol. Geotherm. Res. 285, 247{277}.

Wadati, K., 1933. On the travel time of earthquake waves, Part II. Geophys. Mag. 7, 101–111.

Walck, M.C., 1988. Three-dimensional V p/V s variations for the Coso Region, California. J. Geophys. Res. 93 (B3), 2047. https://doi.org/10.1029/JB093iB03p02047.

Walter, T.R., Amelung, F., 2007. Volcanic eruptions following M≥ 9 megathrust earthquakes: implications for the Sumatra-Andaman volcanoes. Geology 35 (6), 539–542.

Watt, S.F.L., Pyle, D.M., Mather, T.A., 2009. The inluence of great earthquakes on volcanic eruption rate along the Chilean subduction zone. Earth Planet. Sci. Lett. 277, 399–407.

West, F.G., Heiken, G.H., Homuth, E.F., Peterson, R.W., Crowe, B.M., Wohletz, 1978. Tilts Associated with Volcanic Activity Guadaloupe, French West Indies. Fall 1976. LA-7500-MS Informal Report Uc-11. Los Alamos National Laboratories.

White, R., McCausland, W., 2016. Volcano-tectonic earthquakes: a new tool for estimating intrusive volumes and forecasting eruptions. J. Volcanol. Geotherm. Res. 309, 139–155.

Williams, C.A., Wadge, G., 1998. The effects of topography on magma chamber deformation models: application to Mt. Etna and radar interferometry. Geophys. Res. Lett. 25 (10), 1549–1552. https://doi.org/10.1029/98gl01136.

Zlotnicki, J., Feuillard, M., Hammouya, G., 1994. Water circulations on La Soufrière volcano inferred by self-potential surveys (Guadeloupe, Lesser Antilles). Renew of volcanic activity? J. Geomagn. Geoelectr. 46 (1994), 797{813.

Zoback, M., Rummel, F., Jung, R., Raleigh, C., 1977. Laboratory hydraulic fracturing experiments in intact and pre-fractured rock. Int. J. Rock Mech. Min. Sci. and Geomech. 14, 49–58.

Zollo, A., Marzocchi, W., Capuano, P., Lomax, A., Iannaccone, G., 2002. Space and time behavior of seismic activity at Mt. Vesuvius volcano, southern Italy. Bull. Seismol. Soc. Am. 92 (2), 625–640.